Published in final edited form as:
J Geophys Res Planets. 2017 December ; 122(12): 2469–2488. doi:10.1002/2017JE005331.

Oxidative alteration of ferrous smectites and implications for the redox evolution of early Mars

Steven M. Chemtob[1,2], **Ryan D. Nickerson**[2], **Richard V. Morris**[3], **David G. Agresti**[4], **Jeffrey G. Catalano**[2]

[1]Department of Earth and Environmental Sciences, Temple University, Philadelphia, PA 19122, U.S.A.

[2]Department of Earth and Planetary Sciences, Washington University, St. Louis, MO 63130, U.S.A.

[3]EIS Directorate, NASA Johnson Space Center, Houston, TX, U.S.A.

[4]Department of Physics, University of Alabama at Birmingham, Birmingham, AL, U.S.A.

Abstract

Surface conditions on early Mars were likely anoxic, similar to early Earth, but the timing of the evolution to oxic conditions characteristic of contemporary Mars is unresolved. Ferrous trioctahedral smectites are the thermodynamically predicted products of anoxic basalt weathering, but orbital analyses of Noachian-aged terrains find primarily Fe^{3+}-bearing clay minerals. Rover-based detection of Fe^{2+}-bearing trioctahedral smectites at Gale Crater suggest that ferrous smectites are the unoxidized progenitors of orbitally-detected ferric smectites. To assess this pathway, we conducted ambient-temperature oxidative alteration experiments on four synthetic ferrous smectites having molar Fe/(Mg+Fe) from 1.00 to 0.33. Smectite suspension in air-saturated solutions produced incomplete oxidation (24–38% $Fe^{3+}/\Sigma Fe$). Additional smectite oxidation occurred upon re-exposure to air-saturated solutions after anoxic hydrothermal recrystallization, which accelerated cation and charge redistribution in the octahedral sheet. Oxidation was accompanied by contraction of the octahedral sheet ($d_{(060)}$ decreased from 1.53–1.56 Å to 1.52 Å), consistent with a shift towards dioctahedral structure. Ferrous smectite oxidation by aqueous hydrogen peroxide solutions resulted in nearly complete Fe^{2+} oxidation but also led to partial Fe^{3+} ejection from the structure, producing nanoparticulate hematite. Reflectance spectra of oxidized smectites were characterized by $(Fe^{3+},Mg)_2$-OH bands at 2.28–2.30 μm, consistent with oxidative formation of dioctahedral nontronite. Accordingly, ferrous smectites are plausible precursors to observed ferric smectites on Mars, and their presence in late-Noachian sedimentary units suggests that anoxic conditions may have persisted on Mars beyond the Noachian.

1. Introduction

The present Martian atmosphere is oxic, but the temporal evolution of its redox state from primordial anoxic conditions is unresolved. Some planetary evolution models (Chevrier *et al.*, 2007) suggest that photochemical water splitting and hydrogen escape were prevalent and produced an oxidizing atmosphere as early as the Noachian (approximately 4.1 to 3.7

Gyr ago (Carr & Head, 2010)). In contrast, climate models accounting for heavy volcanic outgassing in the Noachian predict an anoxic Martian atmosphere (Catling & Moore, 2003; Ramirez *et al.*, 2014; Sholes *et al.*, 2017) where volcanogenic gases (H_2S, SO_2, H_2, CO, and CO_2) would have efficiently consumed photochemically produced oxidants. Such anoxic conditions could theoretically have persisted as long as vigorous volcanic activity continued, i.e. into the Hesperian (approximately 3.7 to 3.1 Gyr ago) (Sholes *et al.*, 2017). Petrologic studies of the Noachian-aged Martian meteorite ALH84001 (King & McSween, 2005; Righter *et al.*, 2008) also require anoxic or minimally oxic conditions in the surface and near-subsurface.

The extensive record of H_2O/OH-bearing minerals at the Martian surface, observed *in situ* by rover-based methods and from orbit using visible/near-infrared (VNIR) reflectance spectroscopy, provides constraints on the timing of Martian oxidation. Fe/Mg-bearing phyllosilicates, proposed to form by fluid interaction with basaltic crust in surface and subsurface environments, constitute 89% of exposures of H_2O/OH-bearing phases (Carter *et al.*, 2013; Ehlmann & Edwards, 2014). The thermodynamically favored products of basalt weathering under anoxic conditions are Fe^{2+}- and Mg-bearing smectites (Burns, 1993; Catalano, 2013). Fe^{2+}-Mg smectite formation by aqueous alteration of ferromagnesian minerals has been demonstrated experimentally to occur only under anoxic conditions (Dehouck *et al., 2014*; Dehouck *et al., 2016*; Nickerson *et al., 2016*). Therefore, the detection of a trioctahedral, Fe^{2+}-bearing smectite in sediments analyzed by the Curiosity rover at Yellowknife Bay in Gale Crater (Vaniman *et al.*, 2014; Treiman *et al.*, 2014; Chemtob *et al.*, 2015) potentially supports anoxic conditions at the time of their formation in the late Noachian/early Hesperian.

In contrast to the Fe^{2+}-bearing smectites observed *in situ* at Gale Crater, most orbitally detected Fe-bearing phyllosilicates, including those at Gale Crater, are interpreted to be ferric dioctahedral smectites, e.g., nontronite (Mustard *et al.*, 2008; Poulet *et al.*, 2008; Murchie *et al.*, 2009; Milliken *et al.*, 2010; Poulet *et al.*, 2014). Some nontronite detections, such as those at Valles Marineris, are associated with thick sedimentary units, suggesting subsurface phyllosilicate formation (Roach *et al.*, 2010; Ehlmann *et al.*, 2011). Dioctahedral smectites have also recently been detected *in situ* by Curiosity at Gale Crater in the Murray Formation, upsection from Yellowknife Bay (Bristow *et al.*, 2017).

One available explanation for the prevalence of Martian nontronite is that the smectite is the initial (direct) product of aqueous alteration of Fe^{2+}-rich basalt. This nontronite formation pathway implies co-located chemical oxidants and basalt at the time of oxic alteration. Alternatively, ferrous iron in basalt can oxidize under anoxic conditions during water-rock interaction by reduction of OH/H_2O to H_2, as occurs during serpentinization (Oze & Sharma, 2007). However, formation of fully ferric smectite in anoxic environments is rare; dominant minerals produced during serpentinization are magnetite, Fe^{3+}-bearing serpentine, and, at low temperatures, ferrous or ferroan smectites (Evans *et al.*, 2013; Dehouck *et al.*, 2014; Bristow *et al.*, 2015).

We consider here an alternative scenario in which Fe^{3+}-bearing smectites observed from orbit and detected by *Curiosity* are not initial alteration phases but are instead the products

of oxidation of precursor ferrous smectites formed by anoxic aqueous alteration (Catalano, 2013). Ferrous smectites occur on Earth in altered oceanic crust below the zone in which oxygenated seawater penetrates (Andrews, 1980; Badaut *et al.*, 1985; Alt *et al.*, 1986; Alt & Teagle, 2003) and as alteration products of continental volcanic units (*Koyama et al.*, 1973; Treiman *et al.*, 2014), but are difficult to study because of their instability in the terrestrial atmosphere. Consequently, the spectroscopic properties of ferrous smectites and their oxidation products have been the subject of few studies (Chukanov *et al., 2003*; Treiman *et al.*, 2014; Chemtob *et al.*, 2015). In the modern Martian near-surface environment, oxidants that could drive ferrous smectite oxidation include O_2, ozone (O_3) and hydrogen peroxide (H_2O_2), which are present at low concentrations in the atmosphere (Encrenaz *et al.*, 2012; Mahaffy *et al.*, 2013) and other photochemically produced oxidants, including nitrate (NO_3^-) and perchlorate (ClO_4^-), that occur in detectable concentrations in the Martian soil (Klein *et al.*, 1976; Zent & McKay, 1994; Hecht *et al.*, 2009; Kounaves *et al.*, 2010). While oxidative alteration of ferrous smectites to Fe^{3+}-rich smectites like nontronite is thermodynamically favorable for such species (Catalano, 2013), it has not been established experimentally that these Mars-relevant oxidants will generate ferric smectites from ferrous precursors.

The mechanisms involved in the oxidation of trioctahedral ferrous smectites are poorly characterized in the literature, although structural modifications that occur during reduction of nontronite have been extensively studied (e.g., Stucki & Roth, 1977; Komadel *et al.*, 1995; Manceau *et al.*, 2000; Neumann *et al.*, 2011). Briefly, reduction of Fe^{3+} in ferric smectites to Fe^{2+} is accompanied by Fe migration from cis-octahedral sites to adjacent trans-octahedral sites, forming local trioctahedral domains (Manceau *et al., 2000*; Neumann *et al., 2011*). Fe reduction and migration is often accompanied by dehydroxylation, and structural rearrangements are only partially reversible upon reoxidation, depending on the Fe content of the smectite and the extent of dehydroxylation (Komadel *et al.*, 1995; Neumann *et al.*, 2011). However, it is unclear from previous studies whether these mechanisms also operate during the oxidation of initially trioctahedral ferrous smectites, which contain few octahedral vacancies to accommodate Fe migration. Instead, Fe ejection from the octahedral sheet may be required to facilitate oxidation (Badaut *et al.*, 1985; Decarreau & Bonnin, 1986). In addition, smectite layer charge behavior is not analogous between reduced nontronites and native trioctahedral ferrous smectites. Reduction of Fe^{3+} in nontronites will increase the layer charge, producing a high-charge phyllosilicate. In contrast, oxidation of Fe^{2+} in trioctahedral smectites will lower and possibly neutralize the layer charge. Structural differences between dioctahedral nontronites and trioctahedral ferrous smectites likely produce substantially different redox behaviors.

In this study, ferrous smectites were synthesized and aqueously altered in the presence of two oxidants relevant to current Martian surface conditions, namely O_2 and H_2O_2. Although detected on Mars, nitrate was not chosen as an oxidant for study because NO_3^- has been shown to not oxidize Fe^{2+} in reduced nontronite (Zhao *et al.*, 2015) or ferrous smectite (Beehr & Catalano, 2012). Similarly, perchlorate was not studied because ClO_4^- is not known to react abiotically with dissolved or solid phase Fe^{2+} (Urbansky, 1998). Here we characterize the effects of O_2- and H_2O_2-bearing aqueous solution at terrestrial ambient

temperatures on smectite structure, Fe coordination and redox state, and VNIR reflectance spectral signatures.

2. Methods

2.1. Materials and experimental setup

Four ferrous smectite clay minerals (labeled smectites A, B, C, and D) with Fe/(Mg+Fe) molar ratios from 1.00 to 0.33 were studied (Table 1). The smectites were synthesized using a sol-gel method (Decarreau & Bonnin, 1986) that was modified to prevent oxidation of iron (Chemtob *et al.*, 2015). Briefly, amorphous silicate gels were precipitated from reagent solutions in a Coy vinyl anaerobic chamber (97% N_2, 3% H_2, $p(O_2) < 1$ ppm). The anaerobic atmosphere is maintained using palladium catalyst packs. After precipitation, the gels were washed to remove excess salts and then hydrothermally aged at 200° C for 15 days in a vacuum oven, backfilled with N_2 to maintain anaerobic conditions. X-ray diffraction (XRD) and X-ray absorption near-edge structure (XANES) spectroscopy confirmed that the products are smectites with $Fe^{3+}/\Sigma Fe \leq 0.06$, basal (001) spacing between 14 and 16 Å, turbostratic stacking, (060) spacing between 1.53 and 1.56 Å, and unit cell size increasing with increasing octahedral Fe content. The values for (060) d-spacing correspond to trioctahedral stoichiometry (Moore & Reynolds, 1989). Inductively-coupled plasma optical emission spectrometry (ICP-OES) analyses of digested smectites indicated octahedral site occupancies between 2.8 and 3.0.

In air oxidation experiments, 200 to 500 mg of powdered smectite was suspended in ~100 mL of deoxygenated 0.5 *m* $CaCl_2$ solution in the anaerobic chamber. The suspensions were removed from the glovebox and placed on the benchtop under ambient lab conditions (T = 22° C). Capillary tubing connected to a small pump was fed to the bottom of the bottle. Water vapor saturated laboratory air ($P_{O2} = 0.21$) was vigorously bubbled through the solution for 7 days. The $CaCl_2$ solution was used to encourage continuous occupation of the smectite interlayer site by Ca during oxidation and to promote stacking. At the end of the oxidation period, the smectite was returned to the anaerobic chamber, transferred to centrifuge tubes, and separated from the oxygenated solution by centrifugation. After several cycles of washing in deionized, deoxygenated water, the reacted smectites were allowed to air-dry in the nominally anaerobic chamber.

Fe^{2+}-bearing minerals subjected to oxidation then subsequently removed from exposure to the oxidant may continue to undergo transformations due to structural relaxation; however, the timescale of those transformations at ambient temperatures may exceed that which can be feasibly observed experimentally. To accelerate relaxation of disrupted structures post-oxidation, subsamples of two air-oxidized smectites (A and C) were hydrothermally treated at 200° C (recrystallized) for 7 days under anoxic conditions. Recrystallized smectites were then further oxidized in air-saturated solution (reoxidized) for an additional 7 days.

In hydrogen peroxide oxidation experiments, 120 to 160 mg of powdered smectite was introduced to ~25 mL of a 10 mM $CaCl_2$ solution with 0.2% H_2O_2 for 3 days. After treatment, the reacted smectites were separated from the peroxide solution by centrifugation. Preliminary experiments showed that peroxide oxidation caused considerable structural

damage to the smectites (Beehr & Catalano, 2012). To characterize the structures of products post-relaxation, the peroxide-treated smectites were hydrothermally recrystallized in anoxic conditions at 200° C for 7 days.

Post-synthesis oxidation of ferrous smectites in nominally anaerobic chambers is difficult to entirely prevent even at low O_2 concentrations if the reaction is kinetically favored, and we did encounter post-synthesis oxidation for some samples during Mössbauer measurements as previously reported (Chemtob *et al.*, 2015). We also encountered unintentional oxidation under nominally anaerobic conditions in connection with this study (section 3.1); this oxidation complicated but did not obscure interpretation of results related to oxidation by aqueous air-saturated and H_2O_2 solutions.

2.2. Analytical methods

XRD measurements were performed using a Bruker d8 Advance powder diffractometer with a Cu Kα X-ray source and a LYNXEYE XE silicon strip detector. Under anaerobic conditions, smectites were loaded into a sample holder consisting of a recess in a silicon zero diffraction plate, then enclosed within an airtight dome to prevent oxidation. The dome is transparent to the X-ray beam, but displays a broad diffraction feature over the interval 8° to 17° 2θ. Scans were performed over a 2θ range of 3° to 80°. Unit cell parameters were determined by nonlinear least squares fitting of observed diffraction peaks using SixPACK (Webb, 2005), assuming a Voigt peak shape with 50% Gaussian and 50% Lorentzian character.

Structural parameters and average Fe oxidation states of smectites and their oxidized products were determined using Fe K-edge X-ray absorption fine structure (XAFS) spectroscopy, conducted at beamlines 5-BM-D, 12-BM-B, and 13-BM-D at the Advanced Photon Source (APS) at Argonne National Laboratory. All beamlines employed Si(111) double-crystal monochromators and beamline-specific mirror configurations for harmonic rejection. Data were collected simultaneously in transmission and fluorescent yield mode, at incident beam energies ranging from 200 eV below the Fe absorption edge (7112 eV) to 800 eV above the absorption edge (corresponding to $k = 15$ Å^{-1}). This range spanned the XANES region (−30 eV to +50 eV relative to the Fe edge) and extended X-ray absorption fine structure (EXAFS) region (+50 eV to +800 eV). Incident energy was incremented at 5 eV intervals from −200 eV to −50 eV, 1 eV intervals from −50 eV to −10 eV, and 0.25 eV intervals from −10 eV to +30 eV. Above +30 eV, step sized varied with k^2 to allow additional counting time at high k. Total acquisition time was ~50 minutes per XAFS spectrum.

Modeling procedures of EXAFS spectra of untreated ferrous smectites were previously described in Chemtob *et al.* (2015). Raw spectral scans were averaged and normalized using Athena, a graphical user interface for IFEFFIT (Newville, 2001). These normalized EXAFS spectra were k^3-weighted and analyzed in SixPACK. Scattering paths for structural model fitting were derived from the biotite structure using FEFF 7.02 (Ankudinov *et al.*, 1988). Biotite was chosen as a model structure because it contains trioctahedral sheets hosting ferrous iron. Cation sites in trioctahedral sheets are typically distorted and consist of two short cation-oxygen bonds and four long cation-oxygen bonds; these two paths are labeled

Fe-O1a and Fe-O1b, respectively, in our model. Other scattering paths used in modeling include cations in neighboring octahedral sites (Fe-Fe, Fe-Al_{oct}, and Fe-Mg) and Si in the tetrahedral sheet (Fe-Si). Multiple scattering was not modeled. For each scattering path, the coordination number (N), interatomic distance (R), and a Debye-Waller factor representing disorder (σ^2) were determined using nonlinear least squares fitting. For scattering paths from neighboring octahedral sheet cations (Fe-Fe, Fe-Al, and Fe-Mg), values of N were fixed according to smectite stoichiometry. We assumed single values of R and σ^2 for all three octahedral scattering paths. Coordination numbers (N) for Fe-O1a, Fe-O1b, and Fe-Si were fixed at 2, 4, and 4, respectively.

Modeling of EXAFS spectra of oxidized smectites followed a similar procedure. As above, scattering paths were derived from the biotite structure. We also modeled changes in octahedral site occupancy with oxidation, as might occur with transformation to a dioctahedral structure. For simplicity, we fit an occupancy variable, allowed to vary between 0 and 1, that linearly modified the coordination number for Fe-Fe, Fe-Al, and Fe-Mg. In other words, for the purpose of the EXAFS model, we fixed the octahedral Fe/Mg and Fe/Al ratios for the partially oxidized smectites to be equal to that of unoxidized precursors. We fit the Fe-O peak for the partially oxidized smectites using just two shells, as in the ferrous smectites. In reality, six or more Fe-O shells may be present: two shells for Fe^{2+} in trioctahedral coordination, two shells for Fe^{3+} in dioctahedral coordination, and two shells for Fe^{3+} in ferrihydrite and/or nanohematite. EXAFS cannot resolve these shells; however, this fitting procedure does allow detection of average changes in Fe-O interatomic distance. Similarly, derived Fe-Fe distances represent an average of numerous coordination environments (dioctahedral Fe, trioctahedral Fe, and Fe in iron oxyhydroxides) and can be used to track bulk average changes in Fe coordination.

The XANES spectral region was used for determination of average Fe oxidation state and speciation via linear combination fitting (LCF). XAFS spectra of additional materials were collected for use as endmember standards for LCF of the spectra of oxidized smectites. Smectite standards included nontronite NAu-2 ($Fe^{3+}/\Sigma Fe = 1$) and a synthetic ferrous smectite confirmed by MB to have $Fe^{3+}/\Sigma Fe = 0$ (Chemtob *et al., 2015*). Because several oxidized smectite samples are shown by XRD to contain Fe oxides or oxyhydroxides (section 3.2), we also synthesized and collected XAFS spectra for two-line ferrihydrite and hematite for use as LCF standards. Ferrihydrite and hematite were each synthesized following methods from Schwertmann & Cornell (2008).

The XANES measurements of Fe oxidation state were complemented by Mössbauer (MB) spectroscopy. MB spectra were collected using a MIMOS-II instrument, located at NASA Johnson Space Center (JSC) and operating in backscatter measurement geometry at 293 K under desiccating conditions (N_2 gas purge with <100 ppm_v H_2O and <100 ppm_v O_2), except for the peroxide-treated samples which were analyzed under ambient laboratory conditions because XANES measurements indicated the samples were fully oxidized. MB analysis postdated XANES analysis by 3 to 24 months (Table S1). Spectra were velocity-calibrated and fit using a least squares fitting procedure described elsewhere (Agresti *et al.*, 2006; Agresti & Gerakines, 2009). Briefly, peak areas and peak widths of doublet pairs were constrained to be equal during fittings. For the spectra that featured hematite sextets, center

shift and quadrupole splitting were constrained to literature values (0.37 mm/s and −0.20 mm/s, respectively) (Morris *et al.*, 1995) because of low peak intensities. Where the fitting model included two ferric doublets, the peak width for the two doublets were constrained equal. The recoil-free fraction ($f(Fe^{3+})/f(Fe^{2+})$) was set to 1.21 after De Grave & Van Alboom (1991) and Morris *et al.* (1995), who found that value to be valid for a mineralogically diverse range of Fe-bearing samples.

Visible and near-infrared (VNIR) reflectance spectra were collected using Analytical Spectral Devices (ASD) spectrometers at Washington University (WU) and at JSC over the range 0.35 to 2.5 μm. At both sites, spectra were collected using a reflectance probe attachment that contains its own light source; a Spectralon 99% diffuse reflectance standard was also analyzed to correct the smectite spectra to absolute reflectance. WU spectra were collected shortly after the conclusion of each oxidation experiment. VNIR spectra at WU were collected in ambient air (295 K, ~40% RH); subsamples of the smectites were heatsealed during transport from the anaerobic chamber to the spectrometer and were opened to air for a maximum of 3 minutes before analysis. Repeat VNIR analyses over a 2–3 minute period showed no detectable changes in spectral properties over that time. VNIR analyses at JSC were conducted immediately following each MB analysis. At JSC, VNIR spectra were collected under the same desiccating conditions as the MB measurements, except for the peroxide-treated samples, which were analyzed under ambient laboratory conditions (295 K, ~54% relative humidity (RH)).

3. Results

3.1. Characterization of redox state of oxidation products

Peroxide treatment caused nearly-complete Fe^{2+} oxidation ($Fe^{3+}/\Sigma Fe \geq 0.97$) in all four smectite samples. In the two peroxide-treated smectites for which both XANES and MB data were collected (C and D), redox determinations by the two methods were in excellent agreement (Table 1). Exposure to air-saturated solution resulted in incomplete oxidation of all four ferrous smectites. Modeling of XANES and MB spectra of samples oxidized in air-saturated solution suggests $Fe^{3+}/\Sigma Fe$ contents between 0.24 and 0.80 (Tables 1–2; Figures 1–2). However, large discrepancies between XANES-derived and MB-derived $Fe^{3+}/\Sigma Fe$ contents were observed for several samples (O_2-oxidized A, O_2-oxidized B, and O_2-oxidized D).

The differences in measured redox state between XANES and MB could be attributable to systematic error in the collection or modeling of one or both spectral datasets, although both techniques have have been used extensively for quantification of Fe oxidation state in silicates (e.g., Bajt *et al.*, 1994; Morris *et al., 1995*; Wilke *et al., 2005*). One source of potential error in Fe redox state from XANES linear combination fitting is incorrect selection of spectral endmembers. Fe coordination environment, as well as redox state, affects Fe K-edge position; thus, LCF fitting using standards that do not closely match the Fe speciation of our standards could introduce systematic errors in $Fe^{3+}/\Sigma Fe$. However, our LCF fits show isosbestic behavior relative to selected standards, consistent with negligible mismatch in Fe coordination environment. Incorrect selection of the recoil-free fraction could also cause systematic biases in MB-derived $Fe^{3+}/\Sigma Fe$, but the selected value has

previously been shown to be valid for a range of Fe-bearing mineralogical samples (Morris *et al.*, 1995). In any case, differences between the two methods were observed in both directions, and thus do not appear to be the result of any systematic error in measurement.

We instead attribute the differences to inadvertent exposure of some sample aliquots to oxygen during storage and transport. During MB analysis, samples were exposed to the N_2 purge gas which has ~80 ppm O_2. Additionally, the seals on some polyethylene bags used for sample transport from WU to APS and from WU to JSC may have leaked, or O_2 diffusion may have occurred through the walls of the polyethylene bags. Differences in Fe redox state between sample aliquots intended for MB and XANES analysis are corroborated by VNIR reflectance spectroscopy, which we take as evidence that the differences are not tied to MB and XANES data analysis methods. The VNIR spectra collected at WU shortly before XAFS analysis show marked differences in peak position corresponding to differences in oxidation state from the VNIR spectra collected at JSC at the same time as MB (Section 3.3).

Following the interpretation that the smectites were subject to inadvertent oxidation, we interpret both XANES- and MB-derived values of $Fe^{3+}/\Sigma Fe$ as upper limits on the extent of Fe^{2+} oxidation at the conclusion of the oxidation experiments. Consequently, we assume the minimum value of $Fe^{3+}/\Sigma Fe$ derived from the two methods corresponds to the redox state at time of experimental completion. On this basis, 7 days of exposure of the four smectites to air-saturated solutions resulted in 24–38% Fe^{2+} oxidation. After hydrothermal recrystallization and re-exposure to air-saturated solutions, oxidation to Fe^{3+} was more complete. Re-oxidized smectites A and C had $Fe^{3+}/\Sigma Fe$ of 94% and 42%, respectively.

3.2. Structural changes with oxidation

3.2.1. Oxidation of Fe^{2+}-rich smectites in air-saturated solution—Oxidation of the most Fe-rich smectites (A and B) in air-saturated solution caused significant lattice contraction, as shown in XRD patterns by the shift of their (060) d-spacings to smaller values, from 1.564 to 1.558 Å and 1.552 to 1.540 Å, respectively (Table 3; Figure 3c). This octahedral sheet contraction is consistent with the oxidation of structural Fe^{2+} to the smaller Fe^{3+} (Manceau *et al.*, 2000). Recrystallization and reoxidation of smectite A led to further contraction of $d_{(060)}$ to 1.525 Å, similar to $d_{(060)}$ values observed for dioctahedral nontronite (Moore & Reynolds, 1989). EXAFS shell fitting supports the interpretation of a contracting octahedral sheet. Fe^{2+} in unaltered trioctahedral smectites is coordinated in a distorted octahedral site with an average Fe-O distance of ~2.10 Å (Chemtob *et al.*, 2015; Manceau *et al.*, 1998; Gates *et al.*, 2002; Bonnin *et al.*, 1985). For smectites A and B, EXAFS modeling implies that the average Fe-O distance decreased with air oxidation to 2.04 and 2.06 Å, respectively. Distances to neighboring cations in the octahedral and tetrahedral sheet (Fe-(Fe,Mg,Al,Si)) also contracted upon oxidation (Table 4; Figure 4a,b).

Although a smectite phase is present after all oxidative treatments of the Fe-rich smectites A and B, XRD and EXAFS demonstrate that a significant fraction of Fe^{3+} is ejected during oxidation in air-saturated solution. Peaks associated with nanoparticulate hematite (14 to 20 nm particle size from the Scherrer equation) are apparent in XRD patterns of recrystallized and reoxidized smectite A (Figure 3a). Mössbauer spectra of recrystallized smectite A also

indicate the presence of hematite; a sextet is present, consistent with ~12% of total Fe in the sample occurring as Fe^{3+} hematite particles with diameters greater than ~7 nm (e.g. Morris *et al.*, 1995) (Table 2). Nanoparticulate hematite likely formed by recrystallization of an X-ray amorphous Fe^{3+} phase (e.g., ferrihydrite) produced by ejected Fe during oxidation. Fourier transformed EXAFS (FT-EXAFS) data indicates a drop in the magnitude of the Fe-(Fe,Mg,Al,Si) peak with oxidation, consistent with partial Fe ejection (Figure 4; Table 4). After recrystallization and reoxidation, smectite A is characterized by shorter Fe-O distances (~1.99 Å) and a less distorted Fe-O shell consistent with Fe primarily in a dioctahedral sheet.

3.2.2. Oxidation of mixed Fe-Mg smectites in air-saturated solution—Unlike the more Fe^{2+}-rich smectites, the mixed Fe-Mg smectites (C and D) showed little change in $d_{(060)}$ upon oxidation in air-saturated solution, recrystallization, and reoxidation (Figure 3c; Table 3). The absence of a lattice contraction is likely a consequence of lower initial Fe^{2+} concentrations in the octahedral sheet. That is, changes in Fe ionic radius with oxidation had little effect on crystallographic unit cell size because Fe was a less abundant component. Additionally, reoxidized smectite C had lower $Fe^{3+}/\Sigma Fe$ (0.42) than smectite A (0.94), further decreasing the fraction of octahedral cations that underwent bond length contraction.

In contrast to the XRD-derived $d_{(060)}$, which was unchanged by air oxidation, the EXAFS-derived average Fe-O distance in smectites C and D decreased (e.g., from 2.08 Å in unoxidized smectite C to 2.05 Å and 2.02 Å, respectively, for oxidized and reoxidized smectite C) (Figure 4; Table 4). These measurements suggest that octahedral Mg controls the overall unit cell dimension but, locally, Fe octahedra contract with oxidation as cation charge increases. The absence of nanoparticulate hematite in the XRD patterns (Figure 3b) and no detectable change in magnitude of the Fe-(Fe,Mg,Al,Si) peak in FT-EXAFS spectra (Figure 4c; Table 4) suggests that minimal Fe^{3+} ejection occurred during air oxidation of the mixed Fe-Mg smectites.

3.2.3. Oxidation of ferrous smectites by hydrogen peroxide solutions—XRD patterns for all four peroxide-treated smectites after recrystallization have values of $d_{(060)}$ (1.520 to 1.524 Å) that are consistent with dioctahedral ferric smectites (Table 3). The result implies oxidation by peroxide solutions is more disruptive to the smectite structure than oxidation by air-saturated solutions. After recrystallization, the XRD patterns of all four peroxide-treated smectites contain peaks for nanoparticulate hematite, consistent with Fe^{3+} ejection (Figure 3a–b; Figure S1). Mössbauer spectra of peroxide-treated smectites C and D also display a nanoparticulate hematite sextet, in agreement with XRD patterns (Figure 5; Table 2). EXAFS spectra were collected for peroxide-treated smectites C and D only (Figure S2; Figure 4). Shell fitting for those spectra indicates that, relative to untreated smectites, peroxide-treated smectites have shorter average Fe-O distances (1.99 Å) and a less distorted Fe-O shell consistent with a dioctahedral structure (Figure 4c–d; Table 4). EXAFS shell fits also show a significant loss of neighboring cations with peroxide treatment. In smectite C, the Fe-Fe coordination number decreased with peroxide treatment from 3.2 (for unaltered sample) to 1.6±0.6 (Table 4). This decrease is larger than would be expected solely from a

structural transition from trioctahedral to dioctahedral and likely indicates Fe^{3+} ejection from the octahedral sheet.

3.3. Reflectance spectroscopy

VNIR spectral properties of unaltered trioctahedral ferrous smectites were described by Chemtob *et al.* (2015). Broad absorption bands centered near 0.70, 0.91, and 1.11 μm in the unaltered trioctahedral smectites (Figure 6) result from Fe^{2+} and Fe^{3+} electronic transitions and Fe^{2+}-Fe^{3+} charge-transfer transitions. The band near 1.4 μm results from stretching overtones of OH bound to octahedral cations and from the OH stretch in adsorbed and interlayer H_2O. The band near 1.9 μm is produced by stretching plus bending combination vibrations of interlayer and adsorbed H_2O. The features in the 2.1 to 2.5 μm region result from combination and overtone bands of trioctahedral (MMM-OH) and dioctahedral (MM-OH) groups (M = Fe^{2+}, Fe^{3+}, Mg^{2+}, and Al^{3+}). The positions of these bands vary with octahedral sheet stoichiometry (Figure 7; Table 5) (Chemtob *et al.*, 2015). Briefly, the band positions assigned to combination vibrations of $(Fe^{2+},Mg)_3$-OH range from 2.353 μm for the Fe^{2+}-rich endmember smectite A to 2.318 μm for the Mg-rich smectite D. The AlAl(Fe^{2+},Mg)-OH feature changes position, from 2.255 μm to 2.245 μm, with decreasing Fe^{2+}/Mg ratio. The OH stretching overtone feature also changes position, from 1.418 to 1.405 μm, with decreasing Fe^{2+}/Mg ratio.

The VNIR spectral properties of ferrous smectites changed significantly upon Fe^{2+} oxidation (Figures 6–7; Table 5). The most oxidized samples (re-oxidized A and all peroxide-treated smectites) are characterized by a band minimum near 0.87 μm, a relative reflectivity maximum near 0.78 μm, an inflection near 0.55 μm, and elevated albedo longward of the ferric absorption edge (~0.55 to ~0.78 μm) (Figure 6; Table 6). These spectral features taken together are characteristic of hematite (e.g., Morris *et al.*, 2000), and we attribute them to the nanoparticulate hematite detected in our XRD and Mössbauer data rather than to smectite Fe^{3+} electronic transitions, which are apparently masked by hematite spectral features. However, the MM-OH and MMM-OH spectral features of these oxidized smectites (discussed below) are not masked because hematite does not have spectral features in that region.

Modest changes in VNIR spectral features near 1.4 and 1.9 μm associated with OH and H_2O were observed with oxidation. For smectites A, B, and C, the OH stretching overtone feature increased in intensity with oxidation in air-saturated solution (Figure S3), but did not change position. A shoulder feature observable at 1.375 μm in smectites A and B, perhaps attributable to a stretching overtone of Si-OH, persisted with oxidation. VNIR spectra of the peroxide-treated smectites were collected in ambient laboratory air, so the hydration features at 1.4 and 1.9 μm are intense and dominated by H_2O; the position of the OH stretching overtone feature varies with Fe^{3+}/Mg ratio (Table 5) as discussed next.

Continuum-removed spectra in the 2.1 – 2.5 μm range show that the positions and intensities of the trioctahedral MMM-OH and dioctahedral MM-OH bands also changed in response to oxidation and structural transformation of the smectites (Figure 7). Continuum-removed spectra of the aliquots of air-oxidized Fe-rich smectites A and B that did not experience inadvertent, post synthesis, additional oxidation (i.e. A-air-ox(JSC) and B-air-ox(WU) in

Figure 7) are broadly similar to their untreated counterparts, i.e., spectrally dominated by Fe^{2+}. The corresponding spectra for smectites A, B, and D that did receive additional oxidation are plotted as dashed lines.

The continuum-removed spectrum of re-oxidized smectite A is distinctly different from its unaltered precursor. The $(Fe^{2+})_3$-OH band is absent, and an additional band centered near 2.28 μm is observed and assigned to dioctahedral $(Fe^{3+})_2$-OH consistent with XRD patterns (Table 3) and MB spectra that show Fe is present predominantly as Fe^{3+} ($Fe^{3+}/\Sigma Fe = 0.94$; Table 1). For comparison, corresponding spectra are shown for ferric smectite SWa-1 and nontronite NAu-2 (Figure 7). The spectra of the inadvertently oxidized, Fe^{3+}-rich aliquots of air-oxidized smectites A and B (i.e. A-O_2-ox(WU) and B-O_2-ox(JSC)) also lack a $(Fe^{2+})_3$-OH band and display bands near 2.28 μm that we attribute to $(Fe^{3+})_2$-OH (dashed lines in Figure 7).

The VNIR spectra of the mixed Fe-Mg smectites C and D after oxidation in air-saturated solution are similar to the spectra of their untreated counterparts. The spectra of recrystallized and reoxidized smectite C also resemble the untreated sample but are characterized by an additional broad shoulder near 2.30 μm (Figure 7). The shoulder is attributed to partial Fe^{2+} oxidation (from $Fe^{3+}/\Sigma Fe = 0.27$ to 0.42; Table 1) with preservation of the trioctahedral structure (Table 3) or a mixed di- and tri-octahedral smectite where the 2.30 μm band is associated with dioctahedral $Fe^{3+}(Fe^{3+},Mg)$-OH (e.g., Bishop *et al.*, 2002). The latter interpretation is supported by the spectrum of peroxide-treated smectite C, which has a well-defined 2.30 μm band (Figure 7; described below).

All untreated and air-oxidized, recrystallized, and re-oxidized smectites have a spectral feature as a shoulder to well-defined minimum near 2.191 μm. A shoulder feature at a similar wavelength was previously observed in spectra of a Fe-rich aluminous smectite by Bishop *et al.* (2008). This band may represent an OH combination mode associated with Al clusters in the octahedral sheet, and was previously assigned to AlAl-OH by Chemtob *et al.* (2015). In smectite C, the 2.191 μm feature diminished in intensity with recrystallization and reoxidation.

The spectra of all peroxide-treated smectites feature a strong band located between 2.284 and 2.298 μm that is assigned to dioctahedral $Fe^{3+}(Fe^{3+},Al,Mg)$-OH (Figure 7). The band position increases with increasing Mg/Al ratio (Table 5). The dioctahedral structural assignment also follows from the XRD patterns (Table 3; Figure 3). Therefore, the peroxide-treated smectites are nontronite with variable octahedral contributions from Al and Mg. Although we do not know the relative proportions of Fe^{3+}, Mg, and Al because of ejection of Fe^{3+} from the smectite structure during oxidation, the spectra for Mg-poor peroxide-treated A and B are very similar to those for ferric smectite SWa-1 and nontronite NAu-2 (Figure 7). We attribute the shoulder at 2.316 μm in peroxide-treated smectite D to relatively more octahedral Mg compared to peroxide-treated A and B. Other spectral features include a band at 2.24 μm, assigned to (Al,Fe^{3+})-OH, and a band at 2.40 μm commonly assigned to stretch-translation modes of $(Fe^{3+},Mg)_2$-OH (Gates *et al.*, 2002; Frost *et al.*, 2002) (Figure 7).

4. Discussion

4.1. Mechanisms of ferrous smectite oxidation

During oxidation in air-saturated solution, none of the ferrous smectites studied reached fully ferric compositions. The resistance of the ferrous smectites to complete oxidation after extended exposure to O_2 may relate to their trioctahedral structure. Iron oxidation in dioctahedral smectites has been proposed to be kinetically limited by cation migration required to maintain charge balance in the octahedral sheet (Manceau *et al.*, 2000; Gorski *et al.*, 2012). Trioctahedral smectites contain few octahedral vacancies to accommodate these structural rearrangements. Progressive Fe^{2+} oxidation in trioctahedral smectites may lead to positive charge buildup in the octahedral sheet. In the absence of charge redistribution by cation migration, each instance of Fe oxidation causes progressively stronger electrostatic repulsion and, therefore, increasing energetic unfavorability of further oxidation. Gorski *et al.* (2012) observed that in electrochemical reduction and reoxidation experiments, a significant fraction of octahedral Fe in Fe-rich smectites NAu-1 and NAu-2 was redox-inactive, presumably requiring extreme applied potentials to react. Similarly, a fraction of the Fe in the ferrous smectites of this study may not be labile under air-oxidizing conditions.

Another mechanism that may also explain incomplete oxidation is surface passivation. Since Fe^{3+} migration through the octahedral sheet is sluggish, Fe^{3+} forming at the edges of the smectite particles may form a passivating layer and limit further oxidation. Ilgen *et al.* (2012) attributed the observed inhibition of As^{3+} oxidation by the nontronite NAu-1, after initially fast reaction, to the passivation of the nontronite surface by formation of Fe^{3+}oxide moieties.

In contrast to air-saturated solutions, peroxide solutions fully oxidize structural Fe in the ferrous smectites. Peroxide has a higher redox potential than O_2, such that Fe oxidation will proceed more readily even as positive charge buildup occurs in the octahedral sheet. Additionally, Fe^{2+} oxidation by peroxide proceeds by the Fenton reaction (Zepp *et al.*, 1992), in which hydroxyl radical and superoxide radical are produced:

$$Fe^{2+} + H_2O_2 \rightarrow Fe^{3+} + HO\bullet + OH^-$$

$$Fe^{3+} + H_2O_2 \rightarrow Fe^{2+} + HOO\bullet + H^+$$

These radical species are powerful oxidants that may react with structural Fe^{2+}, causing further oxidation.

Oxidation of trioctahedral, ferrous smectite was coupled with transformation to a dioctahedral structure. One mechanism by which octahedral site occupancy can decrease towards $\frac{2}{3}$, as required for a dioctahedral smectite, is irreversible ejection of Fe^{3+} from the octahedral sheet (Farmer *et al.*, 1971; Decarreau & Bonnin, 1986). Ferric iron ejected in this manner form nanoparticulate oxides and hydroxides that can accumulate in the interlayer, plate the surfaces of smectite particles, or develop into crystalline external phases (Farmer *et*

al., 1971; Badaut *et al.*, 1985; Decarreau & Bonnin, 1986; Treiman *et al.*, 2014). In this study, all smectite compositions demonstrated Fe ejection upon peroxide treatment, but only smectites A and B also showed this effect with treatment in air-saturated solution, suggesting that more Fe-rich compositions are more susceptible to loss of structural Fe. One possible interpretation of this compositional dependency is that octahedral $(Fe^{2+})_3$-OH clusters are unstable after oxidation. The untreated ferrous smectites show no tendency towards Fe clustering, i.e., octahedral cations appear to have a random distribution among sites (Chemtob *et al.*, 2015), so the abundance of $(Fe^{2+})_3$-OH clusters should be proportional to the initial octahedral Fe^{2+} content. The oxidation of these clusters to $[(Fe^{3+})_3\text{-OH}]^{3+}$ would create local positive charge accumulation that might promote Fe ejection. In contrast, oxidation of isolated Fe^{2+} octahedra in a predominantly Mg-bearing octahedral sheet may not sufficiently destabilize the smectite structure to cause Fe ejection and iron oxyhydroxide formation.

4.2. Implications of VNIR reflectance spectra for smectite crystal chemistry

Michalski *et al.* (2015) recently characterized variations in the position of MM-OH and MMM-OH bands with smectite crystal chemistry. They determined that for ferric, Fe-rich dioctahedral smectites (molar Fe/Mg > 10), the MM-OH band occurs between 2.284 and 2.290 μm and that for trioctahedral smectites with Fe/Mg < 0.5 the MMM-OH position lies between 2.309 and 2.317 μm. For smectites with molar Fe/Mg ≈ 1, *Michalski et al.* observed a compositional dichotomy; trioctahedral smectites with that ratio had the MMM-OH peak near 2.31 μm, whereas di-trioctahedral smectites had the MM-OH peak near 2.290 μm.

The results of the Michalski *et al.* (2015) study can be compared to our air-reoxidized and peroxide-treated smectites, with the caveat that the Fe/Mg ratios in our oxidized smectites may be lower than in their unaltered counterparts because of Fe^{3+} exsolution and nanohematite formation. Our air-reoxidized and peroxide-treated smectites A and B (unaltered Fe/Mg = ∞ and 8.7, respectively) are dioctahedral and have MM-OH peaks at 2.284 and 2.286 μm, consistent with nontronites having molar Fe/Mg > 10 range as discussed by Michalski *et al.* (2015). For the dioctahedral smectite in peroxide-treated C and D (unaltered Fe/Mg = 1.7 and 0.5, respectively), the octahedral Fe^{3+}-Mg MM-OH band occurs at longer wavelengths (2.295 and 2.299 μm, respectively). Our band positions occur at significantly shorter wavelengths compared to the range reported by Michalski *et al.* (2015) for dioctahedral smectites with Fe/Mg = 0–0.5 (2.310 to 2.316 μm) and at significantly longer wavelengths compared to their range for dioctahedral smectites with Fe/Mg = 1–5 (~2.290 μm). This apparent inconsistency may simply be a sampling problem, because Michalski *et al.* (2015) have only two analyses that overlap the Fe/Mg range for smectites C and D.

A majority (>70%) of Martian smectite detections by CRISM to date feature MM-OH bands near 2.30 μm (e.g., Carter *et al.*, 2013; Ehlmann & Edwards, 2014; Michalski *et al,* 2015). Michalski *et al.* (2015) argue that this ubiquitous detection indicates abundant Martian smectites with Fe/Mg ratios between 5 and 10 which are elevated considerably with respect to unaltered Martian protolith (Fe/Mg ≈ 1.1 (McSween *et al.*, 2009)). Michalski *et al.* (2015) suggest that such enrichment of Fe/Mg may require at least moderately oxic conditions at

the time of basalt alteration. In terrestrial basaltic weathering profiles, atmospheric oxidation state is a critical control on Fe mobility (Rye & Holland, 1998; Babechuk *et al.*, 2014). Under oxic conditions, Fe^{2+} is oxidized and retained in the weathering profile, causing Fe/Mg enrichment. In the absence of oxidants, Fe^{2+} and Mg^{2+} released in the weathering profile behave similarly and are minimally segregated. The crossover atmospheric oxygen level for Fe mobility depends on the rate of influx of weathering acids, but was estimated for terrestrial paleosols as $P_{O_2} \approx 0.0005$ atm by Rye & Holland (1998). Similarly, experimental dissolution of Fe-bearing olivine at $P_{O_2} < 0.0001$ atm produced no fractionation of Fe from Mg in aqueous solution (Sugimori *et al.*, 2012). During seafloor basalt weathering on Earth, other processes such as iron sulfide or oxy-hydroxide precipitation may fractionate smectite Fe/Mg from the protolith composition (Alt *et al.*, 1986; Meunier *et al.*, 2010), but such processes typically require high fluid fluxes and/or input of oxic altering seawater.

Our VNIR spectra suggest that an appeal to Noachian-era oxic conditions resulting in physical separation of Fe from Mg during basalt alteration is unnecessary. The partially oxidized products of our mixed Fe-Mg smectites C and D also have MM-OH band positions near 2.30 μm without physical separation of Fe and Mg. We suggest that CRISM spectral detections of MM-OH bands at 2.30 μm can equally well be explained by oxidation of trioctahedral ferrous smectite with crust-like (~1.1) or even more elevated Fe/Mg ratios to Fe-Mg dioctahedral smectite accompanied by ejection of Fe^{3+} as a ferric-bearing phase (e.g., nanoparticle hematite as in our study). Note that ejection of Fe^{3+} does not change the Fe/Mg ratio for the bulk sample, but does lower the Fe/Mg ratio for the dioctahedral smectite.

4.3. Implications for ferric smectite formation on Mars

Our studies demonstrate that solutions containing aqueous O_2 and H_2O_2, oxidants present in the Martian atmosphere and surficial regolith, can oxidize, over time, trioctahedral ferrous smectite to dioctahedral ferric smectite. Exposure to H_2O_2 aqueous solutions was structurally disruptive to all the smectites studied, ejecting Fe from the octahedral sheet and forming dioctahedral ferric smectite (nontronite) and secondary nanoparticulate hematite. Exposure of smectites to oxygen in air-saturated solutions resulted in nanoparticulate hematite formation for Fe^{2+}-rich smectite compositions but not for mixed Fe-Mg smectites.

Oxidation in air-saturated solution produced fully ferric smectite only after a round of hydrothermal recrystallization, implying that structural relaxation and charge redistribution in the octahedral sheet may be required to produce nontronite from ferrous smectites. Can such structural relaxation occur in the Martian near-surface environment? On Earth, solution recrystallization of smectites occurs most readily in burial diagenesis environments at elevated pressure and temperature. Our experiments demonstrate that rapid recrystallization of smectites in aqueous solutions at 200° C can accommodate additional oxidation, but do not directly constrain the efficacy of this process at lower temperatures and water-rock ratios on geologic timescales. Two pieces of evidence suggest that these reactions can proceed near the arid Martian surface. First, smectite illitization, another structural transformation process that operates either in the solid-state or by dissolution/reprecipitation (Altaner & Ylagan, 1997), has been reported to occur pedogenically at slow rates in arid subaerial or near-

surface environments (Singer, 1989; Bétard *et al.*, 2009). Second, in this study, smectites inadvertently exposed to atmospheric O_2 at low concentrations developed VNIR reflectance spectral features consistent with transformation to nontronite. Although dry air oxidation was not an element of our initial experimental design, its effectiveness suggests that the sustained presence of fluids is unnecessary for Fe^{2+} oxidation and for smectite structural relaxation. Thus, given enough time, Martian near-surface trioctahedral ferrous smectites exposed to oxidants in the atmosphere and regolith likely also undergo structural relaxation towards dioctahedral structures.

VNIR reflectance spectra for the oxidized smectites are distinct from their ferrous trioctahedral precursors and resemble those for dioctahedral ferric smectites (nontronite). Ferrous smectite-bearing rock units later exposed to oxidizing conditions are thus a plausible explanation for widespread remote nontronite detections. Events triggering such a transformation could include 1) ancient exposure to an oxidizing atmosphere; 2) ancient exposure to oxidant-rich solutions like those proposed to have occurred at Meridiani Planum (Hurowitz *et al.*, 2010) or Gale Crater (Rampe *et al.*, 2017); or 3) extended, relatively modern exposure to the current atmosphere after exhumation. Pristine, unaltered ferrous smectites may only be observable by multispectral reflectance imaging at sites where impacts or mass wasting have freshly exposed such phases. The abundance of ferric smectites observed from orbit thus does not necessarily indicate the redox state of the early Martian surface, as oxidative processes would likely overprint any signatures of anoxic conditions in much of the exposed rock record.

4.4. Implications for the redox state of early Mars

Our experiments illustrate that detections of Martian ferric smectites in Noachian terrains need not imply oxidizing conditions during the Noachian because they may be postNoachian oxic alteration products of pre-existing ferrous smectites. Other orbital and rover-based mineralogic observations provide positive evidence for an early anoxic Mars. Near its landing site, the Curiosity rover at Gale Crater observed a gray-colored mudstone (Sheepbed Mudstone) below an oxidized surface layer (Grotzinger *et al.*, 2014; Vaniman *et al.*, 2014), dated to the Late Noachian / Early Hesperian (Grant *et al.*, 2014). The Sheepbed Mudstone was found to contain, among other minerals, trioctahedral smectite and minor iron sulfide (Vaniman *et al.*, 2014). Based on CheMin XRD data, the smectite in the Sheepbed Mudstone was previously interpreted as a ferrian ($Fe^{3+} > Fe^{2+}$) saponite, largely because of equivalence in its (02*l*) d-spacing (4.59 Å) to the terrestrial Griffith saponite (Treiman *et al.*, 2014). The (02*l*) d-spacing of our unaltered smectites C and D (4.60 and 4.58 Å, respectively; Table 3) are within error of the spacing observed for the Sheepbed Mudstone saponite (Vaniman *et al.*, 2014; Chemtob *et al.*, 2015), suggesting that ferrous compositions ($Fe^{2+} > Fe^{3+}$) are also permitted within the constraints of the XRD data. The composition of the Martian saponite could not be calculated independently, but the aggregate chemistry of the saponite plus the amorphous component is more consistent with Mg-rich saponites like Griffith saponite and our two mixed Fe-Mg smectites C and D as opposed to our high-Fe ferrous smectites A and B (Vaniman *et al.*, 2014). The minor amounts of iron sulfides that occur with the Martian smectite (Vaniman *et al.*, 2014) should not persist under conditions of extensive iron oxidation and are perhaps remnants of previously more abundant sulfides.

In Archean rocks on earth, detrital sulfides are interpreted as an indicator of anoxic conditions (e.g. Canfield *et al.*, 2000). This work provides additional evidence that the CheMin analysis of the Sheepbed Mudstone is well explained by the initial formation of a Fe^{2+}-Mg saponite by anoxic basalt alteration, with possible subsequent Fe^{2+} oxidation towards a ferrian composition.

Recent findings of chemical, mineralogical, and redox gradients in the Murray Formation, a mudstone-dominated sedimentary unit upsection from the Sheepbed Mudstone (Grotzinger *et al.*, 2015), provide additional support for precursor ferrous smectites. XRD and evolved gas analyses of upper Murray Formation mudstones indicate that they contain hematite and both dioctahedral and trioctahedral smectites (Rampe *et al.*, 2017; McAdam *et al.*, 2017; Milliken *et al.*, 2017; Bristow *et al.*, 2017). Nontronite (a dioctahedral smectite) has also been detected by CRISM further upslope on Mt. Sharp. (Milliken *et al.*, 2010; Fraeman *et al.*, 2013; Poulet *et al.*, 2014). This mineralogical shift from trioctahedral smectite-bearing downsection units has been interpreted as a Hesperian-aged environmental shift to drier, more oxidizing conditions (Rampe *et al.*, 2017), or as coeval sediments deposited at different depths in a redox-stratified lake (Hurowitz *et al.*, 2017). The assemblage of nontronite and hematite in the Murray Formation is striking because it mirrors the mineral assemblages observed in our experiments. Progressive oxidation of originally Fe^{2+}-smectite-bearing deposits to nontronite, producing iron oxides as a byproduct of Fe ejection, is a potentially plausible mechanism for the Murray Formation mineralogical trend.

Orbital mineralogical datasets also provide evidence for an anoxic early Mars. CRISM has identified abundant and widespread Fe^{3+}-bearing smectites in Noachian and early Hesperian terrains, but only rare and localized exposures of carbonates (Ehlmann & Edwards, 2014). Recent experimental evidence suggests that during aqueous oxic basalt alteration under a CO_2-rich atmosphere, Fe-Mg smectite formation is inhibited in favor of carbonate precipitation (Dehouck *et al., 2016*). Thus, the observed abundance of smectites and paucity of carbonates on Mars could imply poorly oxidizing conditions throughout the Noachian (Dehouck *et al.*, 2016), although the observed relative mineral abundances could also be explained by phyllosilicate formation under mildly acidic conditions which inhibit carbonate stability (Peretyazhko *et al.*, 2016).

CRISM multispectral analysis has identified stratigraphic sequences, at the late Noachian/early Hesperian-dated Mawrth Vallis, Nili Fossae, and other settings, in which Alrich phyllosilicate-bearing units overlie Fe-Mg phyllosilicate-bearing units. These sequences have been interpreted as mega-leaching profiles (Bishop *et al.*, 2008; Ehlmann *et al.*, 2009; Noe Dobrea *et al.*, 2010; Gaudin *et al.*, 2011; Zolotov & Mironenko, 2016). Although the Alrich phyllosilicate-bearing units at Nili Fossae have been proposed to contain iron oxides or oxyhydroxides (Gaudin *et al.*, 2011), the Al phyllosilicate-rich units at Mawrth Vallis are apparently free of ferric phases, implying iron mobility during leaching. In terrestrial weathering profiles, Fe^{3+} is generally more mobile than aluminum, even under oxidizing conditions (Sheldon, 2003; Thomson *et al.*, 2014); however, efficient fractionation of iron from aluminum occurs only in nonoxidizing weathering conditions (Rye & Holland, 1998; Babechuk *et al.*, 2014). Therefore, Late Noachian Fe-Mg phyllosilicate-bearing units likely contained ferrous phases at the time of deposition and leaching, and conditions during

leaching and Al-phyllosilicate formation were insufficiently oxidizing to convert Fe^{2+} to Fe^{3+}.

If ferrous smectites were the initial phyllosilicate constituents of mid- and late-Noachian sedimentary units, anoxic conditions are required at the time of precipitation and deposition. The main driver of the oxidation of the Martian atmosphere is the imbalance between the introduction of reduced hydrogen by volcanic emissions and the non-reversible loss of hydrogen-bearing species (H, H_2, H^+, H_2^+) to space (Lammer *et al.,* 2003). The identification of ferrous smectites in the Gale Crater deposits suggests that the rate of volcanic degassing at the Noachian-Hesperian boundary was sufficient to maintain anoxic conditions, overcoming both consumption of hydrogen by photochemically produced oxidants and hydrogen escape. Average rates of volcanic degassing have been estimated to increase from the late Noachian into the early Hesperian, then drop later in the Hesperian (Craddock & Greeley, 2009). The transition to global oxidizing conditions likely postdates the Yellowknife Bay deposits and may postdate the early Hesperian surge in volcanism. The abundant record of Fe-Mg smectites and the inferred presence of ferrous smectites in large leaching profiles at Mawrth Vallis are consistent with largely anoxic conditions through the late Noachian. The search for life on early Mars should thus in part focus on identifying mineralogical and geochemical signatures consistent with metabolisms that operate under anoxic conditions.

Supplementary Material

Refer to Web version on PubMed Central for supplementary material.

Acknowledgements

This research was supported by the NASA Mars Fundamental Research Program under awards NX11AH09G and NNX14AJ95G. Additional support was provided by the McDonnell Center for the Space Sciences at Washington University. The XRD facility at Washington University is supported by the National Science Foundation under award EAR-1161543. This research used resources of the APS, a U.S. Department of Energy Office of Science User Facility operated by Argonne National Laboratory under contract DE-AC02-06CH11357. We thank Qing Ma (5-BM-D), Sungsik Lee (12-BM-B) and Matt Newville (13BM-D) for assistance with XAFS data collection at APS, and Valerie Fox for assistance with VNIR spectra. Data presented in this manuscript (XRD patterns, Mössbauer spectra, Fe K-edge XAFS spectra, and VNIR reflectance spectra) are available online in the supporting information. This manuscript was greatly improved by thoughtful comments from Erwin Dehouck and two anonymous reviewers.

Works Cited

Agresti DG, Dyar MD, & Schaefer MW (2006). Velocity scales for Mars Mössbauer data, Hyperfine Interactions, 170, 67–74, doi:10.1007/s10751-006-9472-5.

Agresti DG, & Gerakines PA (2009). Simultaneous fitting of Mars Mössbauer data, Hyperfine Interactions, 188, 113–120.

Alt JC, Honnorez J, Laverne C, & Emmermann R (1986). Hydrothermal alteration of a 1 km section through the upper oceanic crust, Deep Sea Drilling Project Hole 504b: Mineralogy, chemistry, and evolution of seawater-basalt interactions, Journal of Geophysical Research, 91, 309–335, doi:10.1029/JB091ib10p10309.

Alt JC, & Teagle DAH (2003). Hydrothermal alteration of upper oceanic crust formed at a fast-spreading ridge: mineral, chemical, and isotopic evidence from ODP Site 801, Chemical Geology, 201, 191–211.

Altaner SP, & Ylagan RF (1997). Comparison of structural models of mixed-layer illite/smectite and reaction mechanisms of smectite illitization, Clays and Clay Minerals, 45, 517–533.

Andrews AJ (1980). Saponite and celadonite in layer 2 basalts, DSDP Leg 37, Contributions to Mineralogy and Petrology, 73, 323–340.

Ankudinov AL, Ravel B, Rehr JJ, & Conradson SD (1998). Real-spacemultiple-scattering calculation and interpretation of X-ray-absorption near-edge structure, Physical Review B, 58, 7565–7576, doi:10.1103/PhysRevB.58.7565.

Babechuk MG, Widdowson M, & Kamber BS (2014). Quantifying chemical weathering intensity and trace element release from two contrasting basalt profiles, Deccan Traps, India, Chemical Geology, 363, 56–75.

Badaut D, Besson G, Decarreau A, & Rautureau R (1985). Occurrence of a ferrous, trioctahedral smectite in recent sediments of Atlantis II Deep, Red Sea, Clay Minerals, 20, 389–404.

Bajt S, Sutton SR, & Delaney JS (1994) X-ray microprobe analysis of iron oxidation states in silicates and oxides using X-ray absorption near edge structure (XANES). Geochimica et Cosmochimica Acta, 58, 5209–5214.

Beehr AR, & Catalano JG (2012). Oxidation pathways of ferrous iron phyllosilicates: insights into Martian phyllosilicate formation, Third Conference on Early Mars: Geologic, Hydrologic, and Climatic Evolution, #7008 (abstr.)

Bétard F, Caner L, Gunnell Y, & Bourgeon G (2009). Illite neoformation in plagioclase during weathering: evidence from semi-arid Northeast Brazil, Geoderma, 152, 53–62.

Bishop J, Madejova J, Komadel P, & Fröschel H (2002). The influence of structural Fe, Al, and Mg on the infrared OH bands in spectra of dioctahedral smectites, Clay Minerals, 37, 607–616.

Bishop JL, Noe Dobrea EZ, McKeown NK, Parente M, Ehlmann BL, Michalski JR, Milliken RE, Poulet F, Swayze GA, Mustard JF, Murchie SL, & Bibring J-P (2008). Phyllosilicate diversity and past aqueous activity revealed at Mawrth Vallis, Mars, Science, 321, 830–833. [PubMed: 18687963]

Bonnin D, Calas G, Suquet H, & Pezerat H (1985). Sites occupancy of Fe^{3+} in Garfield nontronite: a spectroscopic study. Physics and Chemistry of Minerals, 12, 55–64.

Bristow TF, et al. (2015). The origin and implications of clay minerals from Yellowknife Bay, Gale crater, Mars, American Mineralogist, 100, 824–836. [PubMed: 28798492]

Bristow TF, et al. (2017). Surveying clay mineral diversity in the Murray Formation, Gale Crater Mars, Lunar Planet. Sci, vol. XLVIII, 2462, Lunar Planetary Institute, Houston.

Burns RG (1993). Rates and mechanisms of chemical weathering of ferromagnesian silicate minerals on Mars, Geochimica et Cosmochimica Acta, 57, 4555–4574.

Canfield DE, Habicht KS, & Thamdrup B (2000). The Archean sulfur cycle and the early history of atmospheric oxygen, Science, 288, 658–661. [PubMed: 10784446]

Carr MH, & Head JW III (2010). Geologic history of Mars, Earth and Planetary Science Letters, 294, 185–203.

Carter J, Poulet F, Bibring J-P, Mangold N, & Murchie S (2013). Hydrous minerals on Mars as seen by the CRISM and OMEGA imaging spectrometers: Updated global view, Journal of Geophysical Research: Planets, 118, 831–858, doi:10.1029/2012JE004145.

Catalano JG (2013). Thermodynamic and mass balance constraints on iron-bearing phyllosilicate formation and alteration pathways on early Mars, Journal of Geophysical Research: Planets, 118, 2124–2136, doi:10.1002/jgre.20161.

Catling DC, & Moore JA (2003). The nature of coarse-grained crystalline hematite and its implications for the early environment of Mars, Icarus, 165, 277–300, doi:10.1016/S0019-1035(03)00173-8.

Chemtob SM, Nickerson RD, Morris RV, Agresti DG, & Catalano JG (2015). Synthesis and structural characterization of ferrous trioctahedral smectites: implications for clay mineral genesis and detectability on Mars, Journal of Geophysical Research: Planets, 120, 1119–1140. doi:10.1002/2014JE004763.

Chevrier V, Poulet F, & Bibring J-P (2007). Early geochemical environment of Mars as determined from thermodynamics of phyllosilicates, Nature, 448, 60–63, doi:10.1038/nature05961. [PubMed: 17611538]

Chukanov NV, Pekov IV, Zadov AE, Chukanova VN, & Moekkel S (2003). Ferrosaponite $Ca_{0.3}(Fe^{2+},Mg,Fe^{3+})3(Si,Al)_4O_{10}(OH)_2•4H_2O$: A new trioctahedral smectite, Zapiski Vserossiyskogo Mineralogicheskogo Obshchestva, 132, 68–74.

Craddock RA, & Greeley R (2009). Minimum estimates of the amount and timing of gases released into the martian atmosphere from volcanic eruptions, Icarus, 204, 512–526.

De Grave E, & Van Alboom A (1991). Evaluation of ferrous and ferric Mössbauer fractions, Physics and Chemistry of Minerals, 18, 337–342.

Decarreau A, & Bonnin D (1986). Synthesis and crystallogenesis at low temperature of Fe(III) smectites by evolution of coprecipitated gels: Experiments in partially reducing conditions, Clay Minerals, 21, 861–877, doi:10.1180/claymin.1986.021.5.02.

Dehouck E, Gaudin A, Mangold N, Lajaunie L, Dauzères A, Grauby O, & Le Menn E (2014). Weathering of olivine under CO_2 atmosphere: a martian perspective, Geochimica et Cosmochimica Acta, 135, 170–189.

Dehouck E, Gaudin A, Chevrier V, & Mangold N (2016). Mineralogical record of the redox conditions on early Mars, Icarus, 271, 67–75.

Ehlmann BL, Mustard JF, Swayze GA, Clark RN, Bishop JL, Poulet F, Des Marais DJ, Roach LH, Milliken RE, Wray JJ, Barnouin-Jha O, & Murchie SL (2009). Identification of hydrated silicate minerals on Mars using MRO-CRISM: geologic context near Nili Fossae and implications for aqueous alteration, Journal of Geophysical Research, 114, E00D08 doi:10.1029/2009JE003339.

Ehlmann BL, Mustard JF, Murchie SL, Bibring J-P, Meunier A, Fraeman AA, & Langevin Y (2011). Subsurface water and clay mineral formation during the early history of Mars, Nature, 479, 53–60. [PubMed: 22051674]

Ehlmann BL & Edwards CS (2014). Mineralogy of the Martian surface, Annual Review of Earth and Planetary Sciences, 42, 291–315.

Encrenaz T, Greathouse TK, Lefèvre F, & Atreya SK (2012). Hydrogen peroxide on Mars: observations, interpretation and future plans, Planetary and Space Science, 68, 3–17.

Evans BW, Hattori K, & Baronnet A (2013). Serpentinite: what, why, where? Elements, 9, 99–106.

Farmer VC, Russell JD, McHardy WJ, Newman ACD, Ahlrichs JL, & Rimsaite JYH (1971). Evidence for loss of protons and octahedral iron from oxidized biotites and vermiculites, Mineralogical Magazine, 38, 121–137.

Fraeman AA, Arvidson RE, Catalano JG, Grotzinger JP, Morris RV, Murchie SL, Stack KM, Humm DC, McGovern JA, Seelos FP, Seelos KD, & Viviano CE (2013). A hematite-bearing layer in Gale Crater, Mars: Mapping and implications for past aqueous conditions, Geology, doi:10.1130/G34613.34611.

Frost RL, Kloprogge JT, & Ding Z (2002). Near-infrared spectroscopic study of nontronites and ferruginous smectite, Spectrochimica Acta Part A, 58, 1657–1668.

Gates WP, Slade PG, Manceau A, & Lanson B (2002). Site occupancies by iron in nontronites, Clays and Clay Minerals, 50, 223–239.

Gaudin A, Dehouck E, & Mangold N (2011). Evidence for weathering on early Mars from a comparison with terrestrial weathering profiles, Icarus, 2016, 257–268.

Gorski CA, Aeschbacher M, Soltermann D, Voegelin A, Baeyens B, Fernandes MM, Hofstetter TB, & Sander M (2012). Redox properties of structural Fe in clay minerals. 1. Electrochemical quanitification of electron-donating and –accepting capacities of smectites. Environmental Science and Technology, 46, 9360–9368. [PubMed: 22827605]

Grant JA, Wilson SA, Mangold N, Calef F III, & Grotzinger JP (2014). The timing of alluvial activity in Gale crater, Mars, Geophysical Research Letters, 41, 1142–1148, doi:10.1002/2013GL058909.

Grotzinger JP et al. (2014). A habitable fluvio-lacustrine environment at Yellow knife Bay, Gale Crater, Mars, Science, 343, doi:10.1126/science.1242777.

Grotzinger JP et al. (2015). Deposition, exhumation, and paleoclimate of an ancient lake deposit, Gale crater, Mars, Science, 350, doi:10.1126/science.aac7575.

Hecht MH, Kounaves SP, Quinn RC, West SJ, Young SMM, Ming DW, Catling DC, Clark BC, Boynton WV, Hoffman J, DeFlores LP, Gospodinova K, Kapit J, & Smith PH (2009). Detection of perchlorate and the soluble chemistry of Martian soil at the Phoenix lander site, Science, 325, 64–67. [PubMed: 19574385]

Hurowitz JA, Fischer WW, Tosca NJ, & Milliken RE (2010). Origin of acidic surface waters and the evolution of atmospheric chemistry on early Mars, Nature Geoscience, 3, 323–326.

Hurowitz JA, et al. (2017). Redox stratification of an ancient lake in Gale crater, Mars, Science, 356, doi:10.1126/science.aah6849.

Ilgen AG, Foster AL, & Trainor TP (2012). Role of structural Fe in nontronite NAu-1 and dissolved Fe(II) in redox transformations of arsenic and antimony, Geochimica et Cosmochimica Acta, 94, 128–145.

King P, & McSween H (2005). Effects of H2O, pH, and oxidation state on the stability of Fe minerals on Mars, Journal of Geophysical Research, 110, E12S10, doi:10.1029/2005JE002482.

Komadel P, Madejova J, & Stucki JW (1995). Reduction and reoxidation of nontronite: questions of reversibility, Clays and Clay Minerals, 43, 105–110.

Kohyama N, Shimoda S, & Sudo T (1973). Iron-rich saponite (ferrous and ferric forms). Clays and Clay Minerals, 21, 229–237.

Klein HP, Horowitz NH, Levin GV, Oyama VI, Lederberg J, Rich A, Hubbard JS, Hobby GL, Straat PA, Berdahl BJ, Carle GC, Brown FS, & Johnson RD (1976). The Viking biological investigation: preliminary results, Science, 194, 99–105. [PubMed: 17793090]

Kounaves SP, Hecht MH, Kapit J, Gospodinova K, DeFlores L, Quinn RC, Boynton WV, Clark BC, Catling DC, Hredzak P, Ming DW, Moore Q, Shusterman J, Stroble S, West SJ, & Young SMM (2010). Wet chemistry experiments on the 2007 Phoenix Mars Scout Lander mission: data analysis and results, Journal of Geophysical Research, 115, E00E10, doi:10.1029/2009JE003424.

Lammer H, Lichtenegger HIM, Kolb C, Ribas I, Guinan EF, Abart R, & Bauer SJ (2003). Loss of water from Mars: implications for the oxidation of the soil, Icarus, 165, 9–25.

Mahaffy PR, Webster CR, Atreya SK, Franz H, Wong M, Conrad PG, Harpold D, Jones JJ, Leshin LA, Manning H, Owen T, Pepin RO, Squyres S, Trainer M, & MSL Science Team (2013). Abundance and isotopic composition of gases in the Martian atmosphere from the Curiosity rover, Science, 341, 263–266. [PubMed: 23869014]

Manceau A, Chateigner D, & Gates W (1998). Polarized EXAFS, distancevalence least-squares modeling (DVLS), and quantitative texture analysis approaches to the structural refinement of Garfield nontronite, Physics and Chemistry of Minerals, 25, 347–365.

Manceau A, Drits VA, Lanson B, Chateigner D, Wu J, Huo D, Gates WP, & Stucki JW (2000). Oxidation-reduction mechanism of iron in dioctahedral smectites: II. Crystal chemistry of reduced Garfield nontronite. American Mineralogist, 85, 153–172.

McAdam AC, et al. (2017). Constraints on the mineralogy of Gale Crater mudstones from MSL SAM evolved water, Lunar Planet. Sci, vol. XLVIII, 1853, Lunar Planetary Institute, Houston.

McSween HY, Taylor GJ, & Wyatt MB (2009). Elemental composition of the Martian crust, Science, 324, 736–739. [PubMed: 19423810]

Meunier A, Petit S, Cockell CS, El Albani A, & Beaufort D (2010). The Fe-rich clay microsystems in basalt-komatiite lavas: importance of Fe-smectites for pre-biotic molecule catalysis during the Hadeon eon, Origins of Life and Evolution of Biospheres, 40, 253–272.

Michalski JR, Cuadros J, Bishop JL, Dyar MD, Dekov V, Fiore S (2015). Constraints on the crystal-chemistry of Fe/Mg-rich smectitic clays on Mars and links to global alteration trends, Earth and Planetary Science Letters, 427, 215–225.

Milliken RE, Grotzinger JP, & Thomson BJ (2010). Paleoclimate of Mars as captured by the stratigraphic record of Gale Crater, Geophysical Research Letters, 37, L04201, doi: 10.1029/2009GL041870.

Milliken RE, Hurowitz JA, Grotzinger JP, Wiens RC, Gellert R, & Vasavada A (2017). Of elements, minerals, and rocks: Mt. Sharp as a key reference section in assessing the climatic evolution of Mars, Lunar Planet. Sci, vol. XLVIII, 2189, Lunar Planetary Institute, Houston.

Moore DM, & Reynolds RC (1989). X-Ray Diffraction and the Identification and Analysis of Clay Minerals, Oxford Univ. Press, Oxford.

Morris RV, Golden DC, Bell JF III, & Lauer HV Jr. (1995). Hematite, pyroxene, and phyllosilicates on Mars: Implications from oxidized impact melt rocks from Manicouagan Crater, Quebec, Canada, Journal of Geophysical Research, 100, 5319–5328.

Morris RV, et al. (2000). Mineralogy, composition, and alteration of Mars Pathfinder rocks and soils: Evidence from multispectral, elemental, and magnetic data on terrestrial analogue, SNC meteorite, and Pathfinder samples, Journal of Geophysical Research, 105, 1757–1817.

Murchie SL, et al. (2009). A synthesis of Martian aqueous mineralogy after 1 Mars year of observations from the Mars Reconnaissance Orbiter, Journal of Geophysical Research, 114, E00D06, doi:10.1029/2009JE003342.

Mustard JF, et al. (2008). Hydrated silicate minerals on Mars observed by the Mars Reconnaissance Orbiter CRISM instrument, Nature, 454, 305–309. [PubMed: 18633411]

Neumann A, Petit S, & Hofstetter TB (2011). Evaluation of redox-active iron sites in smectites using middle and near infrared spectroscopy, Geochimica et Cosmochimica Acta, 75, 2336–2355.

Newville M (2001). IFEFFIT: Interactive XAFS analysis and FEFF fitting, Journal of Synchrotron Radiation, 8, 322–324, doi:10.1107/S0909049500016964. [PubMed: 11512767]

Nickerson RD, Chemtob SM, & Catalano JG (2016). Clay formation and iron partitioning during anoxic isochemical hydrothermal basalt alteration: implications for formation of Fe smectites on early Mars, Lunar Planet. Sci, vol. XVII, 2458, Lunar Planetary Institute, Houston.

Noe Dobrea EZ, Bishop JL, McKeown NK, Fu R, Rossi CM, Michalski JR, Heinlein C, Hanus V, Poulet F, Mustard JF, Murchie S, McEwen AS, Swayze G, Bibring J-P, Malaret E, & Hash C (2010). Mineralogy and stratigraphy of phyllosilicate-bearing and dark mantling units in the greater Mawrth Vallis/west Arabia Terra area: constraints on geological origin, Journal of Geophysical Research, 115, E00D19, doi:10.1029/2009JE003351.

Oze C, & Sharma M (2007). Serpentinization and the inorganic synthesis of H_2 in planetary surfaces, Icarus, 186, 557–561.

Peretyazhko TS, Sutter B, Morris RV, Agresti DG, Le L, & Ming D (2016). Fe/Mg smectite formation under acidic conditions on early Mars. Geochimica et Cosmochimica Acta, 173, 37–49.

Poulet F, Mangold N, Loizeau D, Bibring J-P, Langevin Y, Michalski J, & Gondet B (2008). Abundance of minerals in the phyllosilicate-rich units on Mars. Astronomy and Astrophysics, 487, L41–L44.

Poulet F, Carter J, Bishop JL, Loizeau D, & Murchie SM (2014). Mineral abundances at the final four curiosity study sites and implications for their formation. Icarus, 231, 65–76.

Ramirez RM, Kopparapu R, Zugger ME, Robinson TD, Freedman R, & Kasting JF (2014). Warming early Mars with CO_2 and H_2, Nature Geoscience, 7, 59–63, doi:10.1038/NGEO2000.

Rampe EB et al. (2017). Mineralogy of an ancient lacustrine mudstone succession from the Murray formation, Gale crater, Mars, Earth and Planetary Science Letters, 471, 172–185, doi:10.1016/j.epsl.2017.04.021.

Righter K, Yang H, Costin G, & Downs R (2008). Oxygen fugacity in the Martian mantle controlled by carbon: New constraints from the nakhlite MIL 03346, Meteoritics and Planetary Science, 43, 1709–1723.

Roach LH, Mustard JF, Swayze G, Milliken RE, Bishop JL, Murchie SL, & Lichtenberg K (2010). Hydrated mineral stratigraphy of Ius Chasma, Valles Marineris, Icarus, 206, 253–268.

Rye R, & Holland HD (1998). Paleosols and the evolution of atmospheric oxygen: a critical review, American Journal Science, 298, 621–672.

Schwertmann U, & Cornell RM (2008). Iron oxides in the laboratory: preparation and characterization, 137 pp., VCH, New York.

Sheldon ND (2003). Pedogenesis and geochemical alteration of the Picture Gorge subgroup, Columbia River basalt, Oregon, GSA Bulletin, 115, 1377–1387.

Sholes SF, Smith ML, Claire MW, Zahnle KJ, & Catling DC (2017). Anoxic atmospheres of Mars driven by volcanism: implications for past environment and life, Icarus, 290, 46–62.

Singer A, (1989). Illite in the hot-aridic soil environment, Soil Science, 147, 126–133.

Stucki JW & Roth CB (1977). Oxidation-reduction mechanism for structural iron in nontronite, Soil Science Society of America Journal, 41, 808–814.

Sugimori H, Kanzaki Y, & Murakami T (2012). Relationships between Fe redistribution and P_{O2} during mineral dissolution under low O_2 conditions, Geochimica et Cosmochimica Acta, 84, 29–46.

Thomson BJ, Hurowitz JA, Baker LL, Bridges NT, Lennon AM, Paulsen G & Zacny K (2014). The effects of weathering on the strength and chemistry of Columbia River Basalts and their implications for Mars Exploration Rover Rock Abrasion Tool (RAT) results, Earth and Planetary Science Letters, 400, 130–144.

Treiman AH, et al. (2014). Ferrian saponite from the Santa Monica Mountains (California, USA, Earth): Characterization as an analog for clay minerals on Mars with application to Yellowknife Bay in Gale Crater, American Mineralogist, 99, 2234–2250.

Urbansky ET (1998). Perchlorate chemistry: implications for analysis and remediation, Bioremediation Journal, 2, 81–95.

Vaniman DT, et al. (2014). Mineralogy of a mudstone at Yellowknife Bay, Gale Crater, Mars, Science, 343, doi:10.1126/science.1243480.

Webb SM (2005). SIXpack: a graphical user interface for XAS analysis using IFEFFIT, Physica Scripta, T115, 1011–1014.

Wilke M, Partzsch GM, Bernhardt R, & Lattard D (2005). Determination of the iron oxidation state in basaltic glasses using XANES at the K-edge, Chemical Geology, 220, 143–161.

Zent AP, & McKay CP (1994). The chemical reactivity of the Martian soil and implications for future missions, Icarus, 108, 146–157.

Zepp RG, Faust BC, & Holgné J (1992). Hydroxl radical formation in aqueous reactions (pH 3–8) of iron(II) with hydrogen peroxide: the photo-Fenton reaction, Environmental Science and Technology, 26, 313–319.

Zhao L, Dong H, Kukkadapu RK, Zeng Q, Edelmann RE, Pentrak M, & Agrawal A (2015). Biological redox cycling of iron in nontronite and its potential application in nitrate removal, Environmental Science and Technology, 49, 5493–5501. [PubMed: 25873540]

Zolotov MY, & Mironenko MV (2016). Chemical models for Martian weathering profiles: Insights into formation of layered phyllosilicate and sulfate deposits, Icarus, 275, 203–220.

Key points:

- Oxidation of trioctahedral ferrous smectites by aqueous O_2 or H_2O_2 produces dioctahedral ferric smectites and Fe oxides or oxyhydroxides
- Oxidation produces systematic changes in VNIR reflectance spectra of ferrous iron-bearing smectites
- Orbitally detected Martian nontronite may be the product of oxidation of ferrous smectite precursors

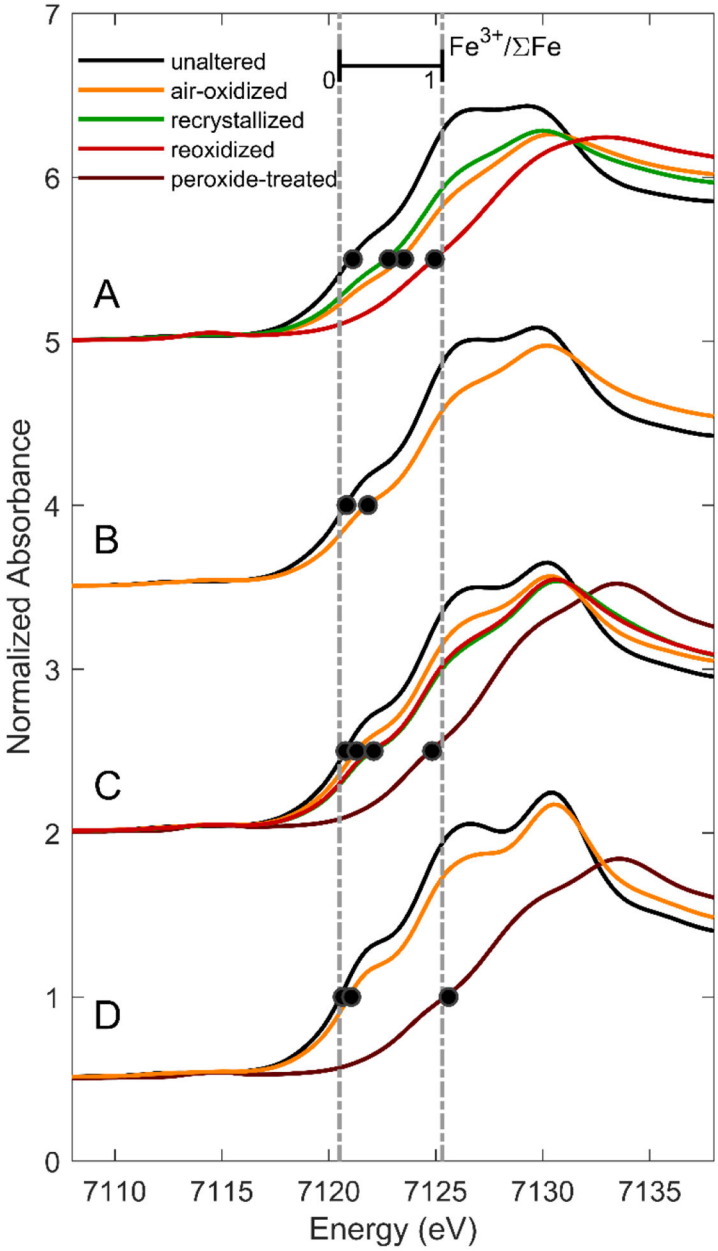

Figure 1.

Fe K-edge XANES spectra of ferrous smectites and their oxidative products, offset for clarity. Fe K-edge positions, defined as the energy at which normalized absorbance is 0.5, are indicated by black dots. Dotted lines at 7120.5 and 7125.3 eV indicate the approximate edge positions corresponding to $Fe^{3+}/\Sigma Fe = 0$ and 1, respectively.

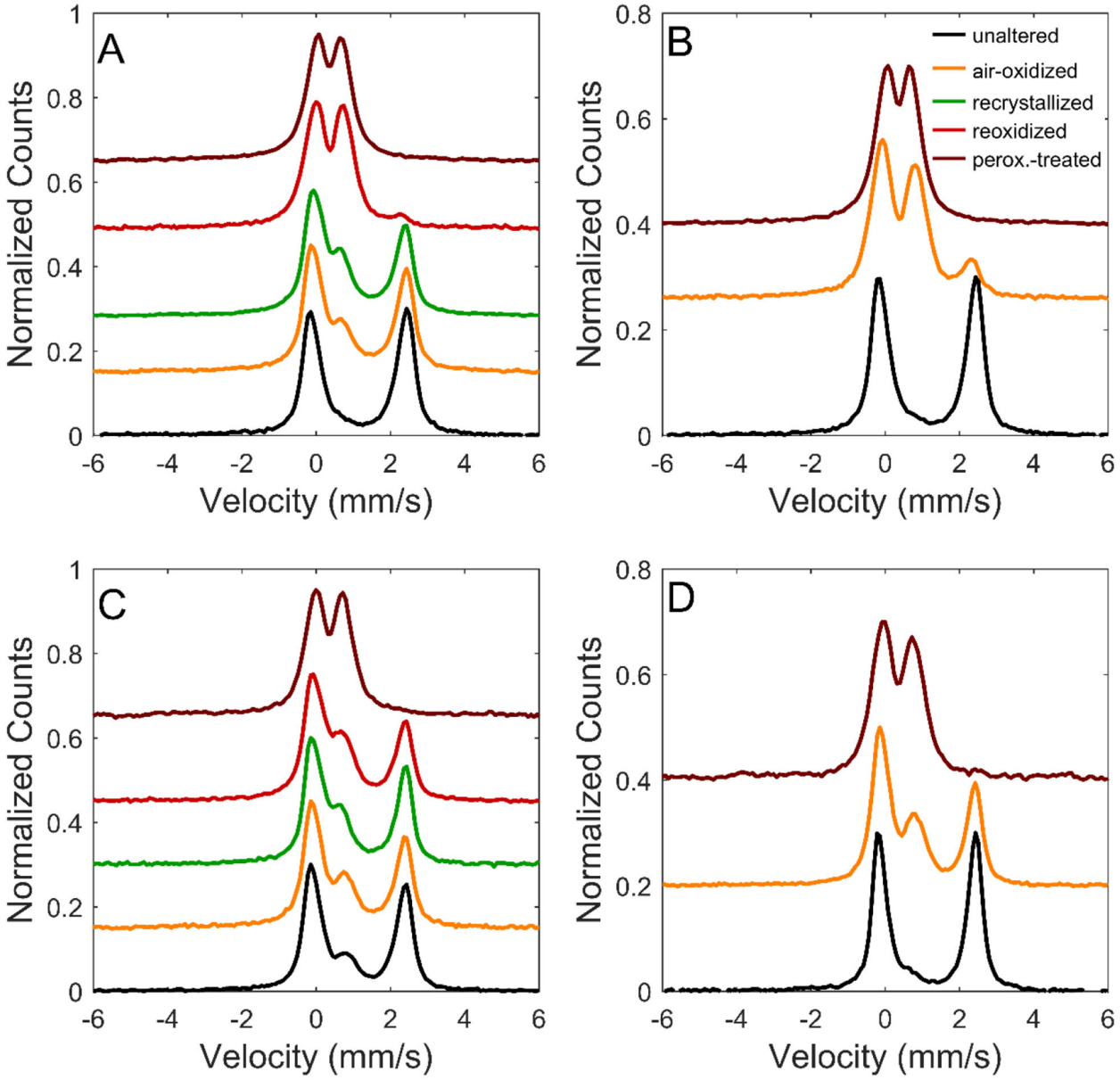

Figure 2.

Backscatter Mössbauer spectra for smectites A, B, C, and D and their oxidation products, offset for clarity. Each spectrum was normalized to a maximum peak intensity of 0.3. Mössbauer spectra of unaltered samples were acquired after some oxidation during storage (cf., Chemtob *et al.*, 2015).

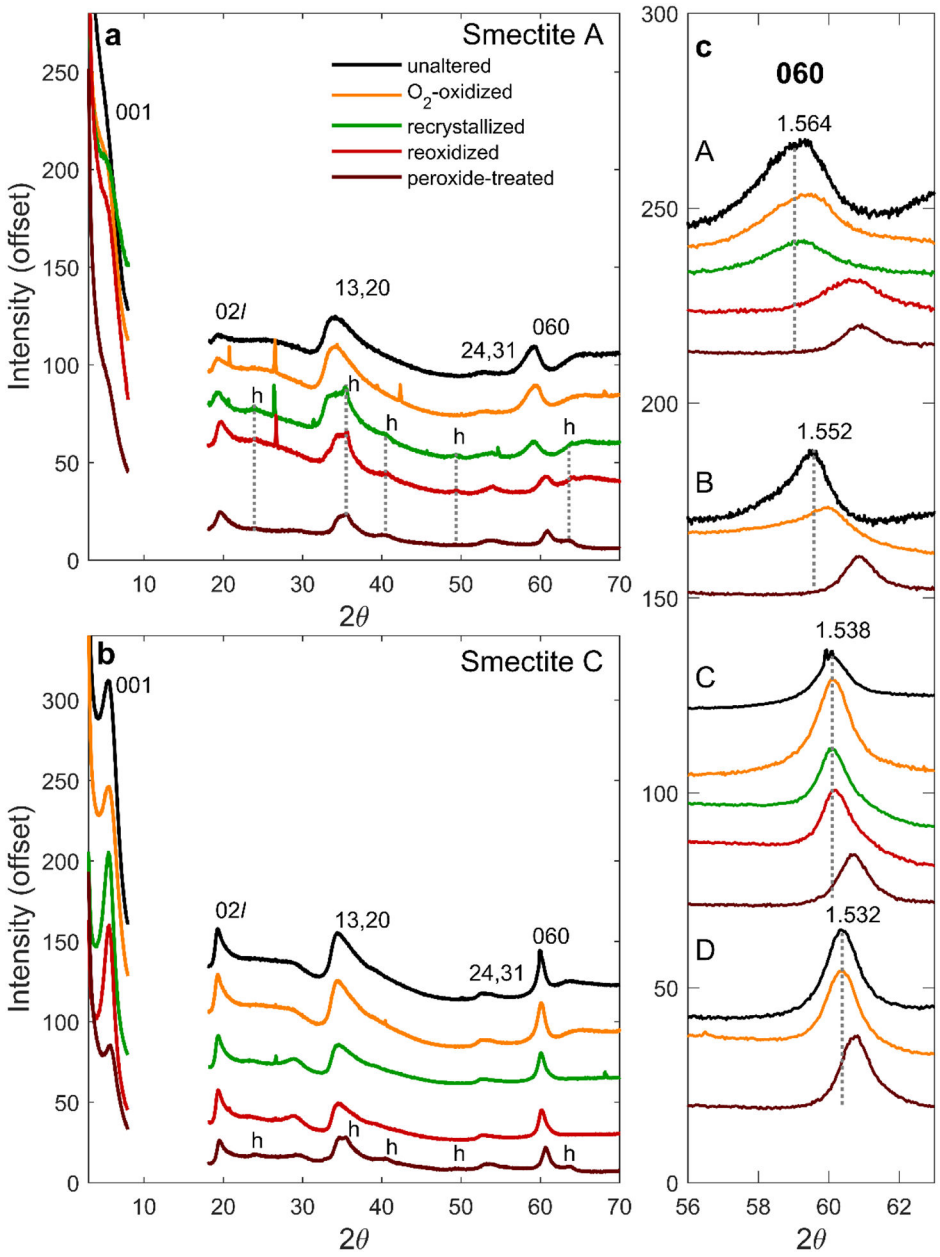

Figure 3.

Cu Kα XRD patterns of smectites and their oxidative products. In (a) and (b), the region from 2θ from 8° to 18° is omitted from the patterns because of a peak produced by the dome of the sample holder. Peaks associated with nanoparticulate hematite are labeled 'h'. Small sharp peaks originate from minor quartz introduced by grinding sample with an agate mortar and pestle. c) The XRD 060 region for samples A, B, C, and D and their oxidative products, with colors as in a). Dotted lines correspond to the 060 peak position for each unaltered sample. d_{060} (in Å) for unaltered samples are also provided.

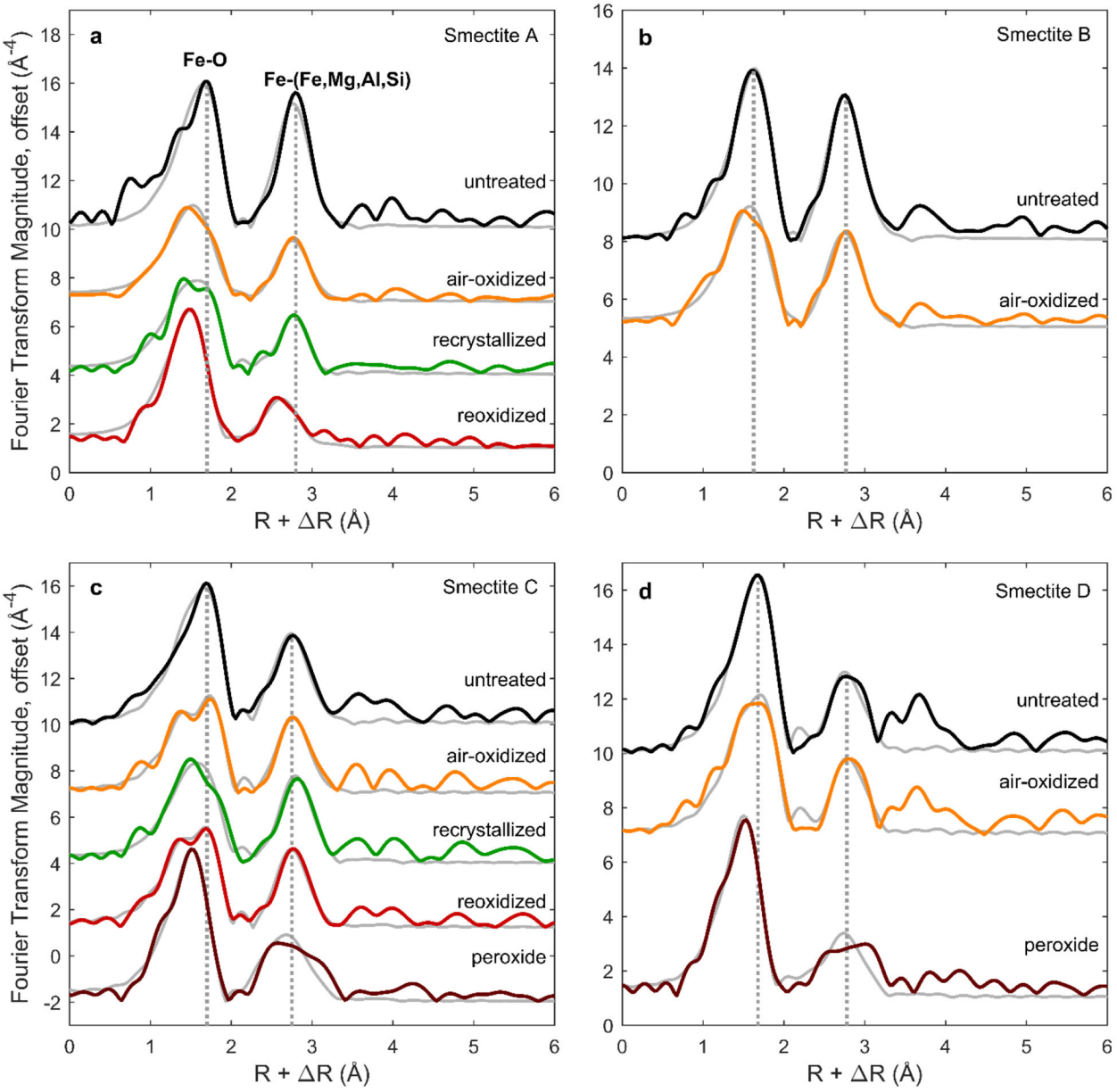

Figure 4.

Fourier transforms of EXAFS spectra, uncorrected for phase shift (ΔR) and offset for clarity. Modeled fits to the EXAFS spectra (gray series) were calculated using the R range from 1 to 3.4 Å. For each composition, dotted lines corresponding to positions of Fe-O and Fe-(Fe,Mg,Al,Si) shells in untreated smectite are included for reference. k^3-weighted EXAFS spectra (prior to Fourier transform) are displayed in Figure S2.

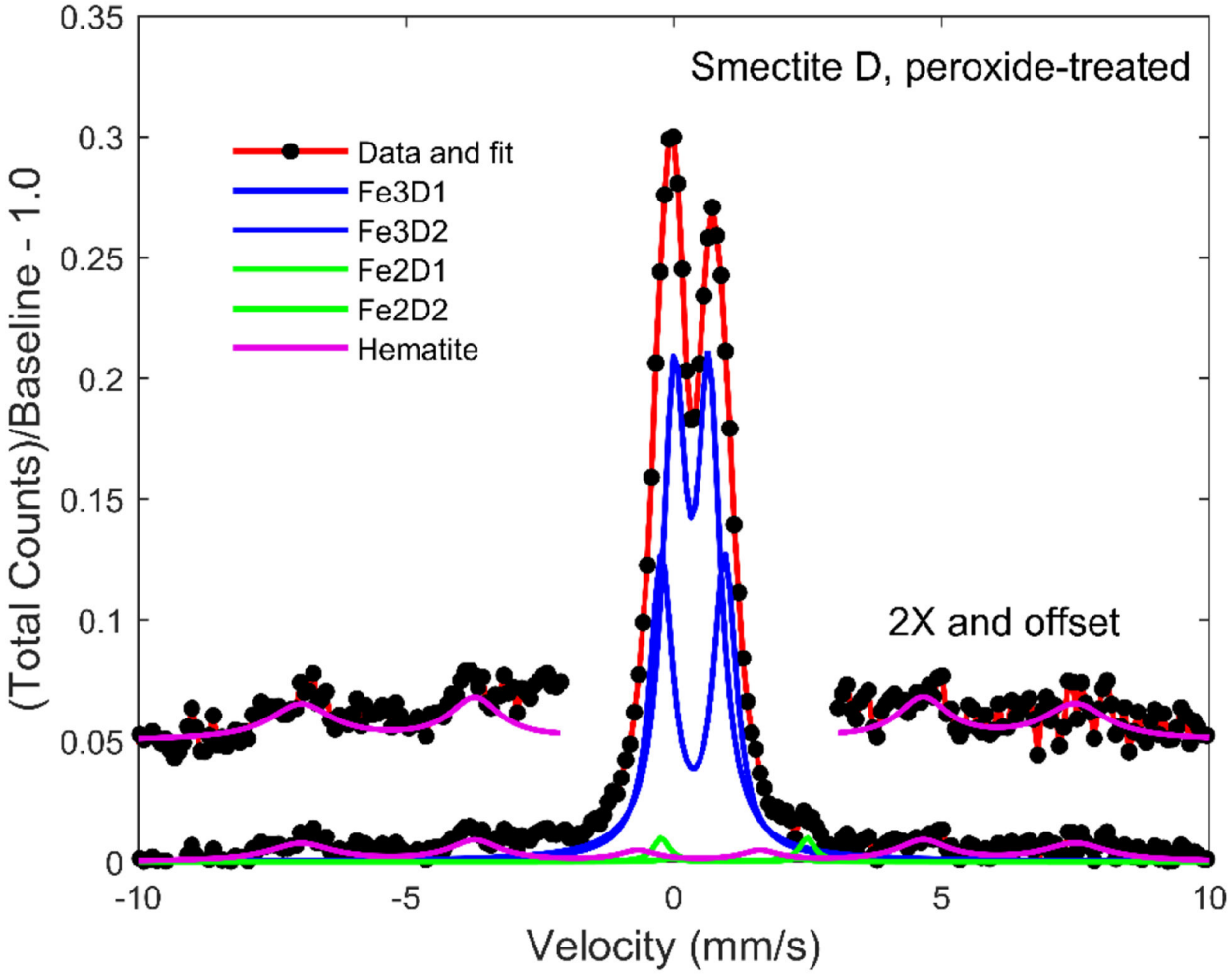

Figure 5.

Mössbauer spectrum, model fit (red trace), and model subspectra for smectite D that was subjected to hydrogen peroxide treatment. Data and hematite fit are also provided in 2x magnification and offset for clarity.

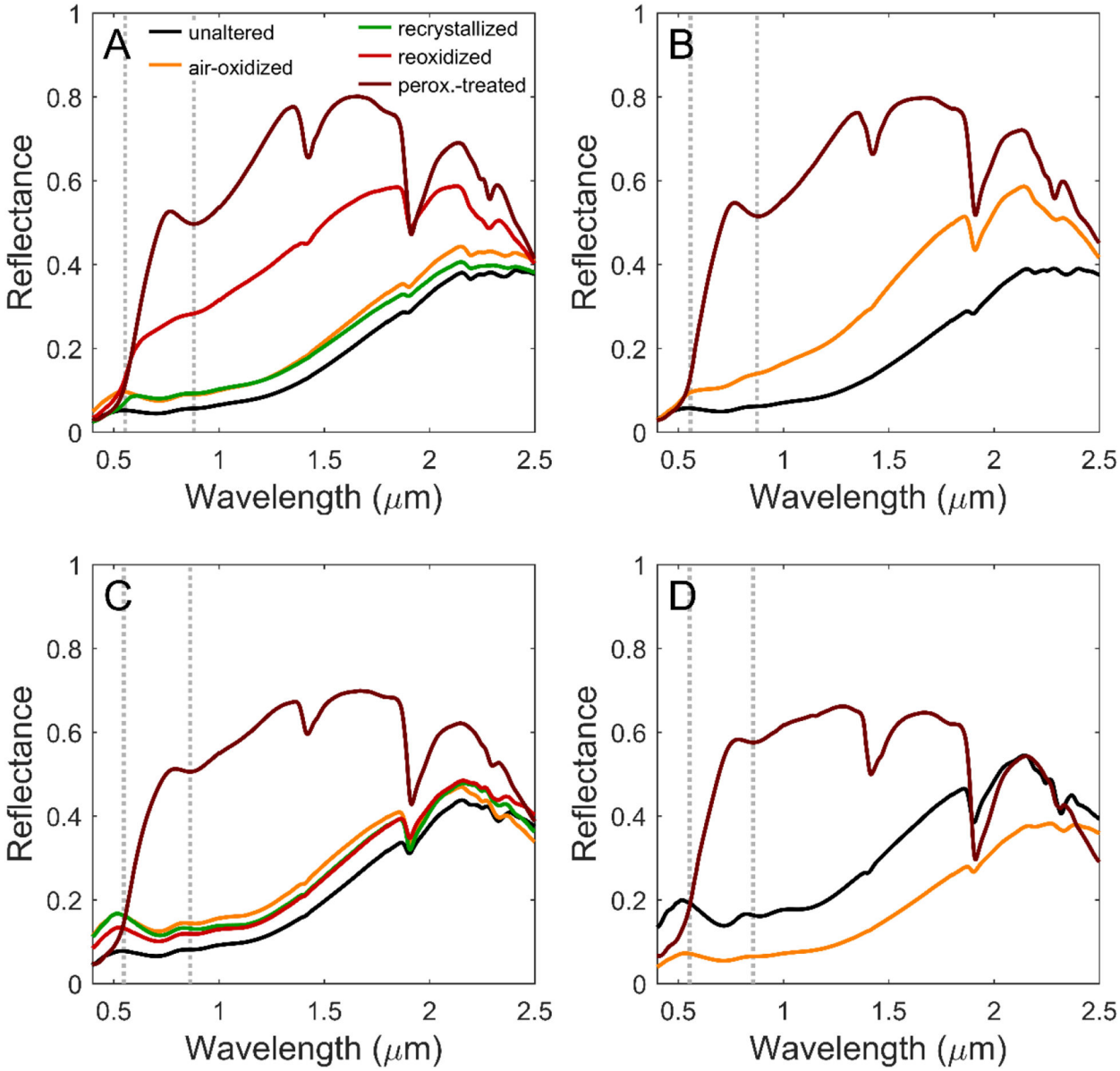

Figure 6.

VNIR reflectance spectra of smectites A – D and their oxidative products, collected in dry anaerobic conditions, except for the peroxide-treated samples which were measured in laboratory air. Gray dotted lines at ~0.55 μm and 0.87 μm highlight the spectral features of Fe3+ in hematite in peroxide-treated smectites.

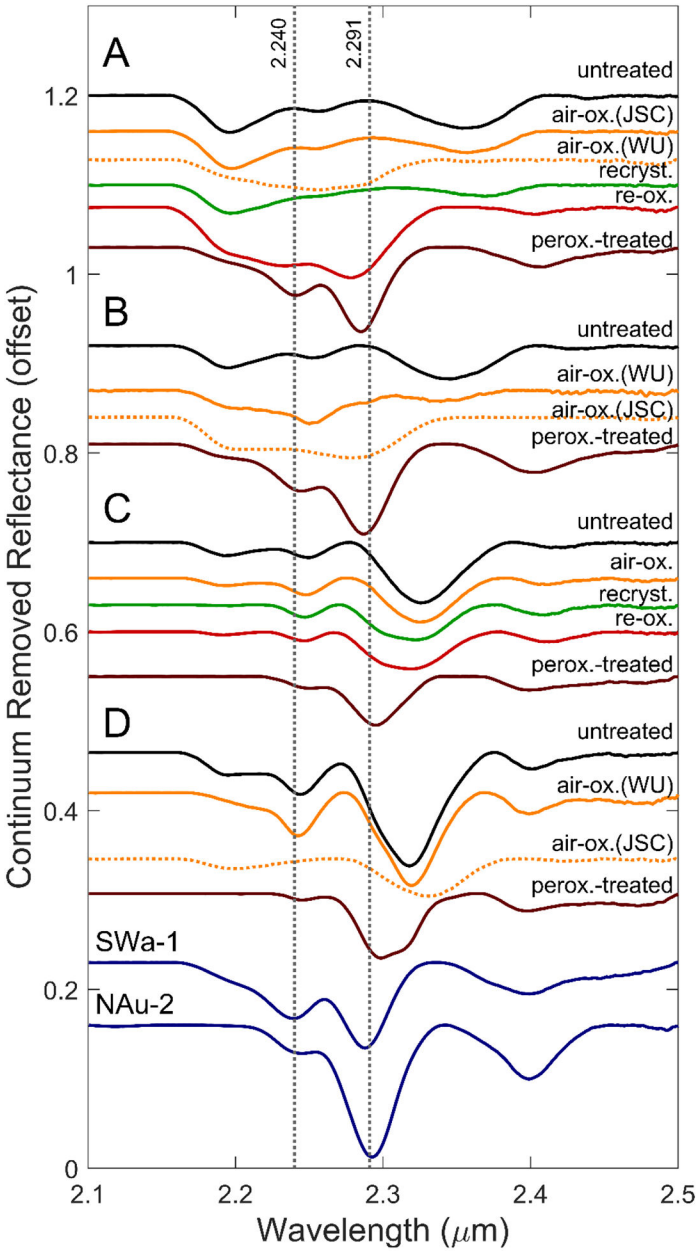

Figure 7.

Continuum-removed visible/near-infrared reflectance spectra, offset for clarity. Spectra of O_2-oxidized samples that experienced additional exposure to air during storage and transport are plotted as dotted lines. The spectra of two smectite standards, nontronite NAu-2 and ferric smectite SWa-1, are included for comparison. Vertical lines at the band minima for $(Fe^{3+}Fe^{3+})$-OH and $(AlFe^{3+})$-OH in nontronite are included for reference.

Table 1.

Smectite compositions and Fe redox state, as determined by XANES and Mössbauer spectroscopy.

			$Fe^{3+}/\Sigma Fe$[b]		
Smectite[a]	**Composition**	**Treatment**	**XANES**[c]	**Mössbauer**[e]	**Minimum**
A (1.00)	$Ca_{0.17}(Fe^{2+}_{2.58}Fe^{3+}_{0.08}Al_{0.27})^{VI}(Si_{3.54}Al_{0.46})^{IV}O_{10}(OH)_2$	unaltered	0.03	0.00	0.00
		air-oxidized	0.57	0.24	0.24
		re-crystallized	0.41	0.38	0.38
		re-oxidized	0.94	0.94	0.94
		peroxide	n.d.[d]	1.00	1.00
B (0.90)	$Ca_{0.18}(Fe^{2+}_{2.36}Mg_{0.27}Al_{0.28})^{VI}(Si_{3.54}Al_{0.46})^{IV}O_{10}(OH)_2$	unaltered	0.00[c]	0.00	0.00
		air-oxidized	0.38	0.80	0.38
		peroxide	n.d.[d]	1.00	1.00
C (0.63)	$Ca_{0.21}(Fe^{2+}_{1.63}Fe^{3+}_{0.09}Mg_{1.01}Al_{0.22})^{VI}(Si_{3.46}Al_{0.54})^{IV}O_{10}(OH)_2$	unaltered	0.05	0.16	0.05
		air-oxidized	0.27	0.30	0.27
		re-crystallized	0.45	0.32	0.32
		re-oxidized	0.43	0.42	0.42
		peroxide	1.00	1.00	1.00
D (0.33)	$Ca_{0.18}(Fe^{2+}_{0.87}Mg_{1.75}Al_{0.28})^{VI}(Si_{3.53}Al_{0.47})^{IV}O_{10}(OH)_2$	unaltered	0.00	0.05	0.00
		air-oxidized	0.24	0.40	0.24
		peroxide	1.00	0.97	0.97

[a] Molar ratio Fe/(Mg+Fe) is given in parentheses.

[b] Uncertainty in $Fe^{3+}/\Sigma Fe$ is ±0.01 for XANES and ±0.02 for Mössbauer.

[c] XANES spectra of unaltered smectite B and nontronite NAu-2 were used as standards for linear combination fitting (LCF); their $Fe^{3+}/\Sigma Fe$ values were defined as 0.00 and 1.00, respectively. $Fe^{3+}/\Sigma Fe$ for other samples was determined by LCF.

[d] No XAFS spectra were collected for peroxide-treated A or B.

[e] Values for unaltered samples from *Chemtob et al.* (2015)

J Geophys Res Planets. Author manuscript; available in PMC 2020 August 14.

Table 2.

Mössbauer Parameters at Room Temperature.

Sample	Smectite A				Smectite B			Smectite C			Smectite D	
Treatment	**air-ox**	**rextll**	**reox**	**perox**	**air-ox**	**perox/ rextll**	**air-ox**	**rextll**	**reox**	**perox/ rextll**	**air-ox**	**perox/ rextll**
$Fe^{3}+/\Sigma Fe$	0.24(2)	0.38(2)	0.94(2)	1.00(2)	0.80(2)	1.00(2)	0.30(2)	0.32(2)	0.42(2)	1.00(2)	0.40(2)	0.97(2)
Ferric Doublet Fe3D1												
CS	0.41(2)	0.36(2)	0.35(2)	0.35(2)	0.37(2)	0.35(2)	0.35(2)	0.41(2)	0.41(2)	0.34(2)	0.40(2)	0.33(2)
QS	0.68(2)	0.72(2)	0.70(2)	0.65(2)	0.79(2)	0.62(2)	0.78(4)	0.57(2)	0.48(4)	0.67(2)	0.66(2)	0.65(2)
FWHM	0.61(2)	0.58(2)	0.54(2)	0.59(2)	0.55(2)	0.58(2)	0.49(2)	0.58(2)	0.59(2)	0.54(2)	0.46(2)	0.51(2)
A	28(2)	31(2)	71(2)	88(3)	56(2)	82(2)	23(2)	36(2)	25(3)	68(3)	27(2)	51(2)
Ferric Doublet Fe3D2												
CS	---	---	0.33(2)	0.32(2)	0.34(2)	0.34(2)	0.34(2)	---	0.40(3)	0.35(2)	0.34(2)	0.36(2)
QS	---	---	1.20(2)	1.11(5)	1.35(2)	1.08(3)	1.25(5)	---	0.93(5)	1.13(3)	1.29(2)	1.18(2)
FWHM	---	---	0.54(2)	0.59(2)	0.55(2)	0.58(2)	0.49(2)	---	0.59(2)	0.54(2)	0.46(2)	0.51(2)
A	---	---	24(2)	12(2)	27(2)	18(2)	12(2)	---	22(3)	21(3)	18(2)	34(2)
Ferrous Doublet Fe2D1												
CS	1.13(2)	1.18(2)	1.20(2)	---	1.12(2)	---	1.16(2)	1.12(2)	1.12(2)	---	1.11(2)	[1.14]
QS	2.39(3)	2.17(2)	2.16(2)	---	2.05(4)	---	2.21(5)	2.39(2)	2.25(5)	---	2.38(2)	[2.36]
FWHM	0.58(2)	0.65(2)	0.31(2)	---	0.38(2)	---	0.59(2)	0.45(2)	0.50(3)	---	0.42(2)	[0.50]
A	49(5)	32(3)	5(2)	---	5(2)	---	36(8)	42(5)	22(4)	---	27(4)	0(2)
Ferrous Doublet Fe2D2												
CS	1.14(2)	1.13(2)	---	---	1.12(2)	---	1.13(2)	1.13(2)	1.13(2)	---	1.15(2)	[1.13]
QS	2.70(2)	2.61(2)	---	---	2.52(2)	---	2.61(2)	2.69(2)	2.63(2)	---	2.66(2)	[2.72]
FWHM	0.34(2)	0.38(2)	---	---	0.38(2)	---	0.36(3)	0.29(2)	0.38(2)	---	0.33(2)	[0.35]
A	24(5)	25(3)	---	---	11(2)	---	30(7)	22(4)	30(4)	---	28(4)	2(2)
Hematite Sextet												
B_{hf}	---	49.1(4)	---	---	---	---	---	---	---	43.6(8)	---	44.8(4)
A	---	12(2)	---	---	---	---	---	---	---	10(3)	---	13(2)

CS = center shift (mm/s) relative to the midpoint of metallic Fe foil at room temperature; QS = quadrupole splitting (mm/s); B_{hf} = hyperfine field strength (T); $Fe^{3+}/\Sigma Fe$ = fraction of total Fe present as Fe^{3+} (corrected for recoil-free fraction, $f(Fe^{3+})/f(Fe^{2+}) = 1.21$); A = fraction subspectral area; FWHM = full width at half-maximum intensity (mm/s); Fixed parameter values (in brackets) for peroxide-treated samples are averages of corresponding entries for samples A through D in Table 5 of *Chemtob et al.* (2015). Uncertainties on final digit(s) of parameters are indicated in parentheses.

Table 3.

XRD *d*-spacings[a]

Smectite	Treatment	d_{001} (Å)	$d_{02\ell}$ (Å)[b]	d_{060} (Å)
A	unaltered	16.19(8)	4.579(6)	1.5636(2)
	air-oxidized	16.99(5)	4.552(3)	1.5584(2)
	re-crystallized	15.18(4)	4.601(5)	1.5617(2)
	re-oxidized	15.76(3)	4.506(3)	1.5249(2)
	peroxide	15.61(4)	4.519(2)	1.5203(1)
B	unaltered	15.55(2)	4.652(3)	1.5523(2)
	air-oxidized	15.10(1)	4.560(2)	1.5400(1)
	peroxide	15.43(1)	4.513(2)	1.5203(1)
C	unaltered	15.67(1)	4.600(2)	1.5385(1)
	air-oxidized	15.61(1)	4.584(1)	1.5381(1)
	re-crystallized	15.87(1)	4.573(1)	1.5378(1)
	re-oxidized	15.76(1)	4.567(1)	1.5358(1)
	peroxide	14.98(1)	4.530(1)	1.5242(1)
D	unaltered	14.78(1)	4.579(2)	1.5321(1)
	air-oxidized	15.66(1)	4.549(1)	1.5318(1)
	peroxide	15.00(1)	4.522(1)	1.5229(1)

[a] Uncertainty for final digit is given in parentheses.

[b] Because of the high asymmetry of the (02ℓ) peak, we report as $d_{(02\ell)}$ the peak fitting results for the (02ℓ) maximum.

Table 4.

Fe K-edge EXAFS structural fitting parameters

Shell		Smectite A unaltered	air-ox	re-xtll	re-ox	Smectite B unaltered	air-ox	Smectite C unaltered	air-ox	re-xtll	re-ox	perox	Smectite D unaltered	air-ox	perox
	N[a]	2	2	2	2	0	2	2	2	2	2	2	2	2	2
Fe-O1a	R[b]	2.016(18)[f]	2.10(13)	1.936(21)	2.084(26)	-	1.963(17)	1.986(19)	1.936(13)	1.951(29)	1.914(13)	2.065(49)	2.011(28)	1.994(30)	2.066(57)
	σ^2 [c]	0.006[g]	0.015	0.009	0.008	-	0.009	0.004	0.006	0.009	0.006	0.008	0.004	0.006	0.008
	N	4	4	4	4	6	4	4	4	4	4	4	4	4	4
Fe-O1b	R[b]	2.140(7)	2.008(38)	2.094(12)	1.943(10)	2.101(7)	2.109(8)	2.124(11)	2.108(10)	2.096(14)	2.080(9)	1.951(11)	2.135(14)	2.132(17)	1.958(12)
	σ^2	0.006(1)	0.0149	0.009(1)	0.008(1)	0.009(1)	0.009(1)	0.004(1)	0.006(1)	0.009(2)	0.006(1)	0.008(3)	0.004(2)	0.006(2)	0.008(3)
	N	5.45	2.6(8)	3.2(1.1)	1.2(7)	4.87	3.6(7)	3.19	3.1(4)	2.6(5)	2.9(4)	1.6(6)	1.80	1.8(2)	0.9(5)
Fe-Fe	R	3.177(22)	3.149(17)	3.218(45)	3.018(28)	3.153(14)	3.139(16)	3.115(18)	3.133(17)	3.136(27)	3.112(18)	2.955(51)	3.095(21)	3.105(18)	3.099(92)
	σ^2	0.012(2)	0.012[i]	0.012	0.012	0.012(2)	0.012	0.011(2)	0.011	0.011	0.011	0.011	0.008(2)	0.008	0.008
	N	0.55	0.28(9)	0.33(10)	0.1(7)	0.57	0.42(8)	0.38	0.38(5)	0.31(6)	0.35(5)	0.18(7)	0.58	0.6(1)	0.11(6)
Fe-Al_{oct}	R	3.177[h]	3.149	3.218	3.018	3.153	3.139	3.115	3.133	3.136	3.112	2.955	3.095	3.105	3.099
	σ^2	0.012[h]	0.012[i]	0.012	0.012	0.012	0.012	0.011	0.011	0.011	0.011	0.011	0.008	0.008	0.008
	N	0	0	0	0	0.56	0.41(8)	2.42	2.4(3)	2.0(4)	2.2(3)	1.2(4)	3.63	3.7(4)	2.2(1.3)
Fe-Mg	R	-	-	-	-	3.153[h]	3.139	3.115	3.133	3.136	3.112	2.955	3.095	3.105	3.099
	σ^2	-	-	-	-	0.012[h]	0.012[i]	0.011	0.011	0.011	0.011	0.011	0.008	0.008	0.008
	N	4	4	4	4	4	4	4	4	4	4	4	4	4	4
	R	3.296(30)	3.278(64)	3.271(35)	3.246(54)	3.304(22)	3.309(29)	3.290(25)	3.276(27)	3.278(21)	3.246(18)	3.252(18)	3.276(27)	3.273(27)	3.226(25)
Fe-Si	σ^2	0.011(7)	0.019(7)	0.007	0.021(1)	0.012	0.013(4)	0.010(4)	.011(3)	0.007(2)	0.009(2)	0.008(2)	0.010(4)	0.010(3)	0.008(3)
	ΔE_0 [d]	−5.0(1.0)	−3.7 (1.8)	−4.7 (1.5)	−2.9(1.6)	−4.8(0.9)	−4.3(1.7)	−6.1(1.7)	−5.7(1.3)	−3.6(1.7)	−6.1(1.3)	−5.4(1.6)	−6.2(2.3)	−4.2(2.4)	−6.3(2.3)
Fe-Oaverage (Å)[e]		2.099	2.039	2.041	1.990	2.101	2.060	2.078	2.051	2.048	2.025	1.989	2.094	2.086	1.994

[a] Coordination number.

[b] Interatomic distance (in Å)

[c] Debye-Waller factor ($Å^2$)

[d] Difference in edge energy between experiment and theory (eV)

[e] Average Fe-O distance = ($N_{Fe\text{-}O1a}$ *$R_{Fe\text{-}O1a}$ + $N_{Fe\text{-}O1b}$ *$R_{Fe\text{-}O1b}$) * 1/6

[f] Statistical uncertainties on last digit(s) in fit parameters are reported in parentheses (1 standard error). Parameters with no listed uncertainties were not varied in the analyses.

[g] The Debye-Waller factor for the Fe-O1a shell was set equal to that for the Fe-O1b shell.

[h] The R and σ^2 parameters for Fe-Al and Fe-Mg were set equal to those for the Fe-Fe shell.

[i] The Debye-Waller factor for Fe-Fe, Fe-Al, and Fe-Mg in the oxidation products were set equal to those for the Fe-Fe shell in the corresponding unaltered sample.

J Geophys Res Planets. Author manuscript; available in PMC 2020 August 14.

Table 5.

VNIR OH combination band positions in micrometers[a].

Smectite	Treatment	H_2O and M_3-OH	AlAl-OH	Al(Fe^{3+},Mg)-OH	AlAl(Fe^{2+},Mg)-OH	(Fe^{3+},Al,Mg)$_2$-OH	(Fe^{2+},Mg)$_3$-OH	(Fe^{3+},Mg)2-OH_{st}[b]	(Fe^{2+},Mg)$_3$-OH_{st}[b]
A	unaltered	1.422, 1.377 (sh)	2.195	---	2.255	---	2.353	---	---
	air-oxidized (JSC)[c]	1.419, 1.376 (sh)	2.197	---	2.258	---	2.356	---	---
	air-oxidized (WU)[c]	1.419	2.20 (sh)	---	2.259	2.275	---	---	---
	re-crystallized	1.421, 1.375 (sh)	2.197	---	2.261	---	2.369	---	---
	re-oxidized	1.424	2.195 (sh)	2.234	---	2.277	---	2.402	---
	peroxide	1.422	2.19 (sh)	2.240	---	2.284	---	2.408	---
B	unaltered	1.418, 1.376 (sh)	2.195	---	2.252	---	2.346	---	2.428(w)
	air-oxidized (WU)[c]	1.418	2.194	---	2.250	---	2.337	---	---
	air-ox. (JSC))[c]	1.418	2.195	---	---	2.272	---	---	---
	peroxide	1.424	---	2.243	---	2.286	---	2.404	---
C	unaltered	1.413, 1.38 (sh, w)	2.191	---	2.249	---	2.325	---	2.413 (w)
	O_2-oxidized	1.412	2.195 (sh)	---	2.247	---	2.324	---	2.411
	re-crystallized	1.412	---	---	2.246	---	2.321	---	2.409
	re-oxidized	1.412	---	---	2.247	---	2.317	---	2.408
	peroxide	1.419	---	2.250	---	2.295	---	2.398	---
D	unaltered	1.406	2.196	---	2.245	---	2.318	---	2.400
	air-oxidized (WU)	1.409	2.196 (sh)	---	2.243	---	2.319	---	---
	air-oxidized (JSC)	1.413	2.199	---	---	---	2.331	---	---
	peroxide	1.413	---	---	2.245	2.298	---	2.396	---

[a] Uncertainty in band positions ±0.003 μm. sh = shoulder, w = weak, and --- = not detected.

[b] Combination OH stretch-translation mode.

[c] Spectra collected at JSC and WU are both included for those samples in which XANES and MB showed different redox states.

Table 6.

Positions of Fe^{3+} spectral features in peroxide-treated smectites in micrometers[a].

Smectite	Inflection	Relative Reflectivity maximum	Fe^{3+} absorption minimum
A	0.554	0.770	0.881
B	0.548	0.766	0.875
C	0.547	0.792	0.863
D	0.498[b], 0.554	0.788	0.856

[a] Uncertainty in band positions ±0.005 μm.

[b] A second inflection point apparent in peroxide-treated smectite D may be attributable to Fe^{3+} in smectite.